7-11-2015

Analysis of the Effect of Thermal Gradients on the Real-time 2D Imaging of the Spot Weld Process.

Andrew Ouellette
University of Windsor

Recommended Citation

Ouellette, Andrew, "Analysis of the Effect of Thermal Gradients on the Real-time 2D Imaging of the Spot Weld Process." (2015). *Electronic Theses and Dissertations.* Paper 5317.

Analysis of the Effect of Thermal Gradients on the Real-time 2D Imaging of the Spot Weld Process.

By

Andrew Ouellette

A Thesis
Submitted to the Faculty of Graduate Studies
through the **Department of Physics**
in Partial Fulfillment of the Requirements for
the Degree of **Master of Science**
at the University of Windsor

Windsor, Ontario, Canada

2015

Analysis of the Effect of Thermal Gradients on the Real-Time 2D Imaging of the Spot Weld Process.

By

Andrew Ouellette

APPROVED BY:

____
Dr. William Altenhof
Department of Mechanical, Automotive and Materials Engineering

____
Dr. Steven J. Rehse
Department of Physics

____
Dr. Roman Gr. Maev, Advisor
Department of Physics

May 14th, 2015

DECLARATION OF ORIGINALITY

I hereby certify that I am the sole author of this thesis and that no part of this thesis has been published or submitted for publication.

I certify that, to the best of my knowledge, my thesis does not infringe upon anyone's copyright nor violate any proprietary rights and that any ideas, techniques, quotations, or any other material from the work of other people included in my thesis, published or otherwise, are fully acknowledged in accordance with the standard referencing practices. Furthermore, to the extent that I have included copyrighted material that surpasses the bounds of fair dealing within the meaning of the Canada Copyright Act, I certify that I have obtained a written permission from the copyright owner(s) to include such material(s) in my thesis and have included copies of such copyright clearances to my appendix.

I declare that this is a true copy of my thesis, including any final revisions, as approved by my thesis committee and the Graduate Studies office, and that this thesis has not been submitted for a higher degree to any other University or Institution.

ABSTRACT

Many monitoring processes have been proposed for the spot weld process, but most of these techniques involve the use of post weld verification methods. An ultrasonic phased array has been shown to be a viable method for the monitoring the spot weld in 2D, however the presence of thermal gradients generated during the welding process can result in a loss of resolution and accuracy within the image. In this report these effects were investigated and the device's imaging ability improved. It was found that the imaging abilities of the device are not severely degraded and that a 0.9 mm resolution is attainable using a 10 MHz phased array. Additionally the maximum 0.2 mm offset of the focused wave generated by heating was found to be correctable by monitoring of the copper water boundary. These results indicate that good potential exists in the future applications of this device.

ACKNOWLEDGEMENTS

Firstly, I would like to thank my colleges in my research group, in particular I would like to thank Andriy Chertov, whose help and experience has helped me accomplish this work, but also Eric Lessard and Tim Mlinaric, who have helped with work related to this project.

I would like to thank the many friends I have made throughout my studies, Russell Putnam, Geoffrey Baran, Jon Fraser, and many others. It is likely I would not have been able to complete my work without their friendship and support.

Lastly I would like to thank my supervisor Dr. Roman Gr. Maev, and the members of my committee, whose helpful comments and input allowed for an increased clarity in this thesis.

Table of Contents

LIST OF TABLES

LIST OF FIGURES

LIST OF APPENDICES

Chapter 1

Introduction and Background Theory

1.1 Introduction

The spot weld process is a widely used technique in the sheet metal joining industry and specifically in the automotive sector[1]. This technique makes use of resistive heating to fuse metal sheets together at a point. Although a common technique, the use of new alloys and metals in an attempt to reduce vehicle weight has resulted in alloys that are more difficult to weld and more likely to encounter issues.

The majority of these issues result from repeated use of the spot weld electrodes causing deformation of the electrode surface, changing the welding conditions. Although remedies such as polishing of the electrode cap to restore the original surface are employed the electrode cap will eventually require replacement. Due to the fact that the electrodes are water cooled, replacement of the caps requires that automated assembly lines be shut down. The expense associated with this often results in the need for balancing weld quality and minimizing downtime.

Due to this extended use of the electrodes, most companies employ some form of testing on the performed welds. Although offline testing methods have been well established, the time requirements means that only a small portion of the welds can be tested. If severe issues are detected at this point an entire batch of welded parts may be scraped[2]. For this reason it is highly desirable to monitor every weld that occurs in real time.

Although a variety of inline testing methods have been proposed to perform this task[3], one technique currently employed in an industrial environment makes use of an ultrasound transducer build into the spot weld electrode[4]. This method, developed within our group, works by monitoring the weld progress using pulsed ultrasound waves. By doing this repeatedly a quality signature of the weld can be created and feedback can be given in real time[5]. Although this system works well in the majority of cases it allows for monitoring only along the center of the weld.

In order to alleviate this constraint a system was developed to allow for acquisition along a cross section of the weld[6], this system was shown to have some success, but was limited to imaging in laboratory conditions. In addition to these limitations the effects of the temperature gradients produced as the sheets are heated was considered negligible. Due to the large gradients produces during welding a quantification of their effects on the imaging process was required to allow for proper assessment of weld quality.

With these limitations in mind, this research was undertaken with two primary goals. First a redesign of the system was needed to improve its imaging abilities and allow for its use outside of laboratory conditions. Secondly the imaging abilities of the system needed to be quantified and the effects of thermal gradients on these imaging abilities determined.

1.2 Overview

This chapter covers the basic principles of welding and discusses the problems that can arise during welding. It covers a method of ultrasonic monitoring that has been developed for use within our group and is the basis for this research.

In Chapter 2 the basics of ultrasound propagation and ultrasound imaging are discussed to familiarize the reader with concepts used in this work. It also introduces the reader to the finite element modelling process employed in this work.

Chapter 3 investigates the limitations of the previously used system and the steps taken to optimize its imaging abilities. It also covers the experimentally determined limitations of the system when imaging the spot weld process.

Chapter 4 covers the effects that the thermal gradients produced during spot welding will have on the imaging process. These effects include changes to both the accuracy and resolution of the system as the weld develop.

Finally Chapter 5 summarizes the abilities and limitations of the system developed. This chapter also summarizes the future potential of the system and the improvements that can still be made.

1.3 The Spot Weld Process

The spot welding process, as outlined in figure 3.1, makes use of two or more metal plates clamped between conductive electrodes, often constructed of copper. Large forces, typically of between 500-1000 N, are applied to the sheets by the electrodes to reduce the contact resistance at the point to be welded. The spot weld controller then allows for the flow of a large current, typically 6000-22000 A in steel, to flow through the metal sheets. This current results in resistive heating, eventually causing melting to occur. At this point the current is turned off and the weld is allowed to cool. Upon solidification the pool of molten metal fuses between the sheets resulting in a joint that can have a comparable strength to the base materials[7]. In order to reduce the damage to the copper electrodes during this process and increase the speed at which subsequent welds can be performed water cooling is typically employed.

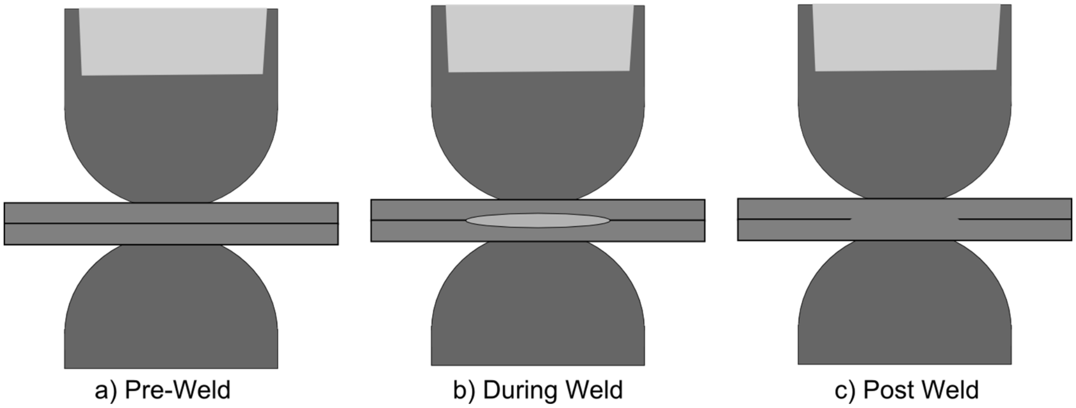

Figure 1.1 - A depiction of the spot weld process at the various stages, prior to welding, during welding and post welding. At the end of welding a fused region is visible in the middle of the stack-up.

In this process, the heat generated within the metal stack is at times difficult to predict due to the presence of multiple metals and the addition of coatings or oxides on the surface of these materials. Although when considered in totality these effects are difficult to describe the basic process is still governed by the underlying physics. In this case the heating within the system occurs through the joule heating effect, as described in equation 1.1, whereby the heat generated Q (in joules) is proportional to the resistance of the metal R, measured in ohms, multiplied by the square of the current, I, in amps and the time for which the current is applied t, measured in seconds.

$$Q_{weld} = I_{weld}^{2} R_{weld} t_{weld} \qquad 1.1$$

During this process, heat flows from the system primarily through basic thermal conduction, described using equation 1.2 below. Whereby the heat flux q (W/m^2) is proportional to the conductivity of the material k(W/m/K) multiplied by the change in temperature.

$$q = -k\nabla T \qquad 1.2$$

1.4 Quality Factors in the Spot Weld

The introduction of new metals and alloys in an effort to decrease vehicle weight and increase fuel efficient has resulted in the use of materials that are difficult to weld and prone to issues. One of the common causes of problems in the spot weld process occurs due to the fact that the electrode caps are used for extended periods of time. During their usage, heating of the copper, high forces and chemical reactions at the surface between the metals results in a degradation of the surface quality[8]. The degradation process is complex, but usually results in changes to the surface size, shape and structure of the cap[8]. This degradation, depicted in figure 2.3 is highly dependent on the materials being welded and the selected welding schedules.

This degradation results in a change in both the force and current distributions that flow through the weld surface, causing a large change in the heating rates and the heat distribution. Although some techniques such as polishing, where the surface of the weld electrode is refinished, can be used to alleviate these effects, the caps will eventually have to be replaced.

Figure 1.2 - The spot weld electrode at increasing stages of degradation, the notable surface changes in the severely degraded cap are a result of material being lost from the cap surface during welding. The rate at which caps degrade is highly dependent on the welding conditions employed.

If the surface area of the caps increases, current density and heating will decrease, resulting in the weld size falling below the manufacturer specifications. In the limit of low heating it is possible to generate welds in which incomplete fusion or no fusion is present between the sheets. These are referred to as stick welds due to the fact that elastic deformation of the metal forms weak bonds, causing the sheets to stick together[9].

If deformation results in a decreased contact area more localized current densities and higher heating will result. As the heat increases within the structure a variety of metallurgical effects can occur, causing the formation of brittle structures within the spot weld that will fail prematurely or in an undesired way. In the extreme internal pressure can exceed the cohesive force of the molten pool. In this situation the molten metal can be expelled from the pool, resulting in a decreased weld size and a reduction in the thickness of the base metal[9]. Unlike undersized welds the effects of overheating and expulsion are harder to characterize. This is due to the fact that the weld size is not the primary limitation in the strength of these welds and failure points are more difficult to determine due to the randomness of expulsion nature.

Other problems that can occur in the spot weld process occur due to the metal used in the process and the heating rate. Although a variety of problems exist the most common are stress cracks and voids that form during the cooling process. Voids are caused by gases becoming trapped within the molten pool, while cracks occur mostly due to brittle alloy formation. Although more random in nature these problems can often be found using current testing methods[9].

1.5 Monitoring Techniques

In order to assess the quality of a spot weld it is common to use monitoring techniques throughout the manufacturing process. When employed frequently, monitoring allows for the detection of the conditions that would result in poor welds and allows for correction of the cause, preventing further issues. Monitoring techniques can be separated into two distinct categories, those performed offline and those performed in-line with the assembly process.

1.5.1 Offline Techniques

Offline techniques for monitoring any process often have a number of advantages due to the fact that they are performed by trained inspectors and allow for the correction of issues that may prevent a proper assessment of weld quality. Due to the amount of existing techniques for offline monitoring, only the ones used in our lab will be discussed, although more complete studies are available[10].

One of the most common techniques used to rapidly assess weld quality in the lab environment is the peel test. In this test two sheets of metal are welded and the weld is peeled back until failure occurs. Depending on the modality of failure and resulting inspection the size of the weld nugget can be determined and the quality of the weld can be assessed in a basic manner. An example of a peeled test sample can be seen in figure 1.4 below, where the resulting weld has failed by tearing out of the base material, allowing for a measure of its size using calipers.

Figure 1.3 - An example of a peel test performed on a weld, the size of the welded area can be measured from the fused region after completion. Although somewhat inaccurate, peel testing is one of the fastest measurement methodologies.

If more information is desired as to the underlying metallurgical structure of the spot weld it is common to perform cross sectioning of the weld sample. In cross sectioning the weld is sliced in half and seated in a resin base. It is then polished to a fine finish and etched in order to highlight varying structures (figure 1.5). By viewing these structures under an optical microscope it is possible to estimate how heating occurred within the weld and the resulting shape of the fused area. If chemical composition is desired the samples can undergo further imaging using x-ray diffraction.

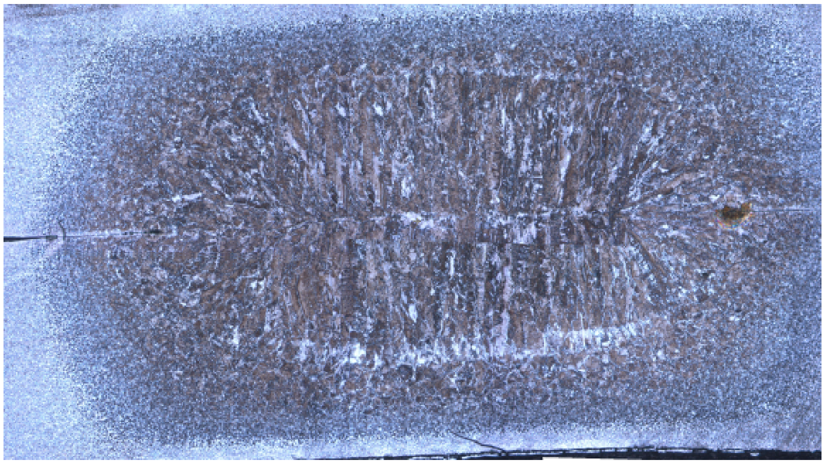

Figure 1.4 - An example of a cross section after chemical etching, the austenitic growths indicate that melting and subsequent solidification has occurred, allowing for a direct measurement of nugget size to occur.

Although these tests allow for a determination of the characteristics of the weld, they require that the weld be destroyed in order to do so. As a result of this they are impractical for testing on more than a select few welds. When welds require testing without destruction non-destructive testing (NDT) are employed. Although a variety of techniques can be used in NDT, ultrasound is one of the most widely employed due to the fact that it allows for visualization of a subject in a safe and cost effective way.

One technique employed in many NDT applications is that of the scanning acoustic microscope. Acoustic microscopy makes use of a higher resolution ultrasound transducer and a mechanical stage to perform a raster scan of an object[11]. In order to accomplish this the part to be imaged must be submerged into a liquid bath to allow for adequate sound transmission. In this method of imaging the region of unfused metal can be imaged using a cross sectional scan. By measuring the region in which no signal is detected from between the plates the total area of fusion can be obtained[12]. Although this technique allows for very high resolution images to be obtained it suffers from the fact that the part being imaged must fit inside the limits of the mechanical stage, often limiting this form of imaging to small parts or portions of a work-piece. For this reason acoustic microscopy is not often used outside of lab samples for weld measurements.

Adaptations of this technique have been implemented using a matrix array transducer. By implementing an element by element scan it is possible to image a region the size of a weld in a rapid manner. As before the welded area is determined by the region in which fusion causes no reflection. An example of such a system is features in figure 1.6 below[10].

Figure 1.5 - The RSWA by Tessonics is an example of a post welding microscopy device. Using a 52 element array the size of a weld is measured using signal processing techniques (Tessonics, 2008).

1.5.2 Inline Techniques

Although offline testing often yields high quality analysis of the weld it must be performed by trained employees or professionals. In the highly automated environments in which spot welding is used this requires an impractical time investment, limiting the evaluative process to select samples. This selective process means that problems can be undetected until after production has concluded, resulting in a large amount of waste product being produced.

For this reason the need for a real time monitoring system is crucial. A real time system can be considered as any system capable of assessing the weld quality in a manner such that production is not significantly affected by its use. Many attempts have been made to adapt offline systems into an automated environment[10], but these systems tend to suffer alignment issues that make their use impractical. Other methods such as monitoring the weld parameters such as voltage, current and electrode displacement have proven to have some effectiveness[10], but suffer from the fact that these parameters are material and setup specific and require calibration in each case. Currently the most promising system for integration in a welding environment is the real time inline spot weld analyzer (RIWA) [13].

The RIWA system was developed within our research group at the University of Windsor. It makes use of a transducer placed inside the water cooling of the electrode to monitor the welding process as it occurs[4], as in figure 1.7. This system works on the principle that the changes in the material that occur during the heating process can be monitored and that direct inference can be made from this knowledge[6]. In order to establish that a good weld has been performed the change from an unwelded to a welded reflection, seen in figure 1.8 is desired. In an ideal condition the weld signature such as that obtained in figure 1.9 results. In this case heating results in a change in the boundary position due to the corresponding change in the speed of sound. At the start of heating the reflection from between the plates splits into the reflection from the top and bottom of the molten pool. These reflections change with respect to the size of the molten pool. After the end of heating the weld begins to cool until the nugget has completely solidified, resulting in reflections only from the top and bottom of the bounded structure.

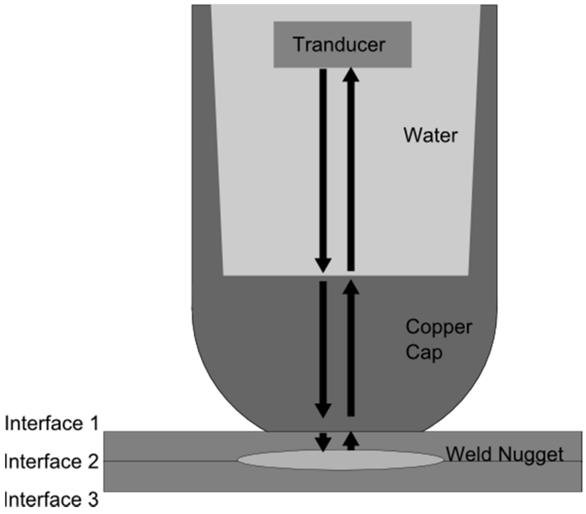

Figure 1.6 -The RIWA monitoring system, consisting of a transducer within the water cooling column and two or more metal sheets. This system allows for weld quality measurements to occur in real-time with little modifications needed to the existing system.

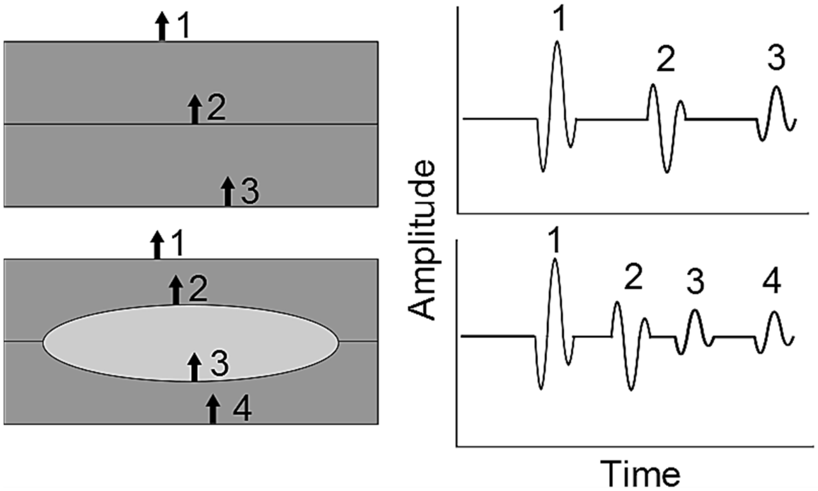

Figure 1.7 - The differing reflections between the unwelded and molten stages of the weld. The transformation of the central reflection into two separate reflections is indicative of melting occurring within the welding stack.

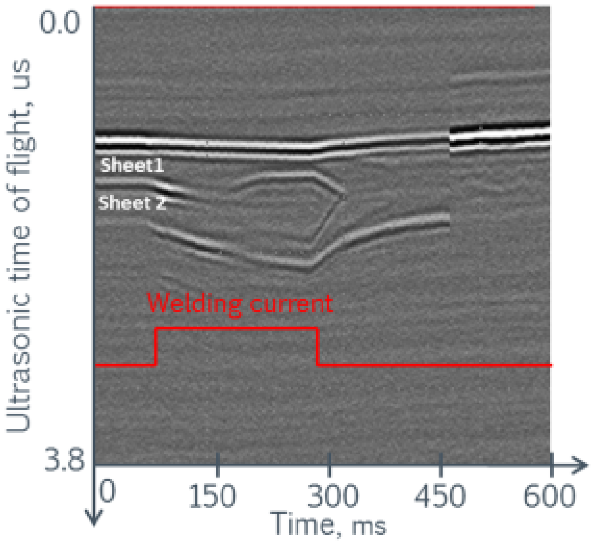

Figure 1.8 – An ideal M-scan, where the development of all boundaries is clearly visible throughout the welding process. Although ideal, the variance between welding setups mean that not all boundaries may necessarily be visible in most cases.

Although the RIWA system has been established as a solution to many problems and is currently used in an industrial environment, the fact that it is limited to imaging the central portion of a weld make its use impractical in some situations. In addition to this the problems it can detect are limited to its region of view. This may not be an issue in many areas, but can cause problems in situations where welds are considered critical. A critical weld can be classified as a weldment whose quality must be dependable for safety concerns. These welds are often limited to areas such as seat belts, but can extend to many regions in the aviation industry. In these cases the use of the RIWA system must often be accompanied by offline inspection.

In order to allow for imaging along more than one dimension the investigation of using a phased array to image the spot weld process was done. Phased arrays, discussed in the next chapter, allow for the use of multiple transducers to scan at points within space. This technique, seen in figure 1.10 was shown to have the potential to allow for multiple signatures to be acquired along the weld surface and a cross sectional analysis to be performed[6]. Although this device allowed for good estimations of the size of spot welds its imaging abilities were unknown and its use was limited to laboratory conditions. This thesis covers the improvements made to the initial design and investigates the limitations of the improved array.

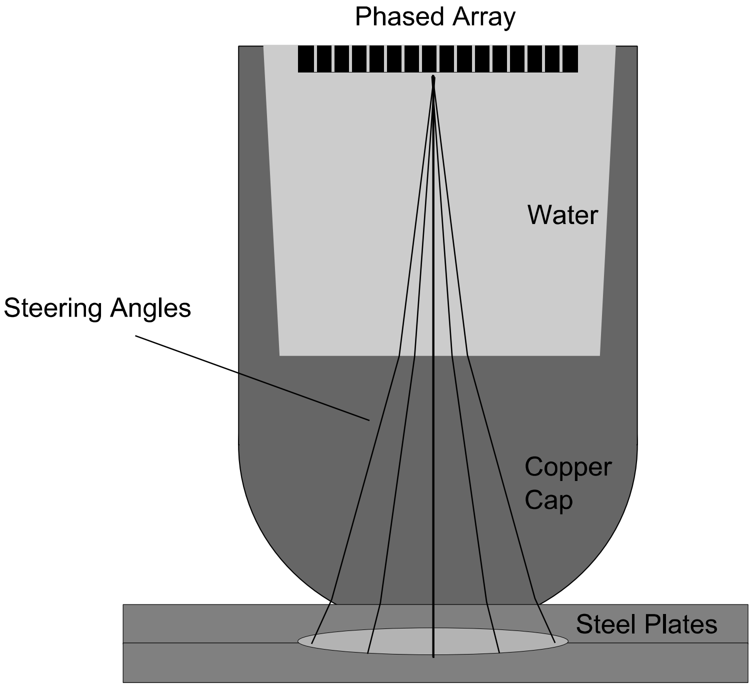

Figure 1.9 - The functionality of the phased array scanning technique. Using phased array imaging techniques, multiple cross sections can be acquired along the welded plates, allowing for far more information than the current RIWA system.

1.6 Spot Welding Model

The finite element model of the spot weld process used in this thesis was developed and tested by a previous student in the group[14]. This model was based off of previously published work[15] and was performed using the COMSOL finite element modelling program. It relies on the use of a coupled electrical thermal model to determine the temperature distributions in the spot weld system. In order to decrease computational time axial symmetric model of the process was employed, allowing for a 2d representation of the system to be used.

In this model the spot weld process is divided into discrete representation of the system by selecting an appropriate spatial mesh. By separating the model into finite steps in time the evolution of the welding model can be found. Using temperature dependent material properties found in a materials product database it is possible to describe the material over the range of temperatures for which welding occurs. For each time step within the model the resistance at each node in the mesh is found. This resistance can be used to calculate the current densities within the model at this point in time. This current flow model is then used with the resistance of the material to allow for the calculation of the heat generation at each point in space. This generated heat is then allowed to propagate through the media for a small amount of time. By starting from the initial welding conditions and slowly repeating the previous processes an accurate model of an idealized spot weld can be created.

In order to verify this model mesh refinement studies were conducted to ensure accuracy in the predicted temperatures. Experimental validation was also performed by extraction of the temperature profile at the axes of the weld. By comparing the expected time of flight between each boundary to those achieved during experimentation the accuracy of the model was found to be in good agreement[15].

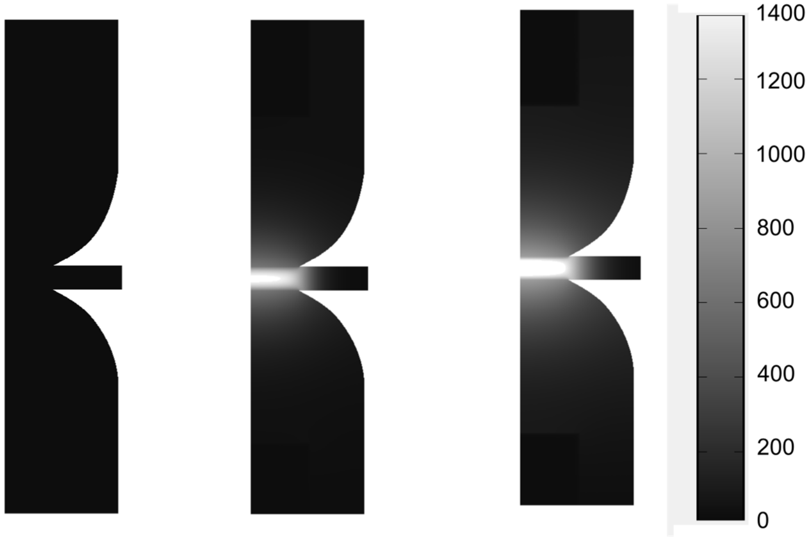

Figure 1.10 - Temperature distributions for the model at the beginning, middle, and end of welding for a 8kA 20 cylce weld, by extracting the values for any given point in time. The thermal gradients present in the system can be determined for arbitrary points in the welding process.

References

[1] N. T. Williams, J. D. Parker, *Review of resistance spot welding of steel sheets Part 1 Modelling and control of weld nugget formation, International Materials Reviews*, Vol 49, No 2, DOI: 10.1179/095066004225010523, (2004).

[2] J. D. Cullen, N Athi, M. A. Al-Jader, A. Shaw, A. I. Al-Shamma'a. *Energy Reduction for the spot welding process in the automotive industry*. Sensors and their Applications XIV, Journal of Physics: Conference Series 76. (2007).

[3] S. Rivas, R. Servent, Tecnitest Ingenieros SL, Madrid, Spain;
J. Belda, Eines, Valencia, Spain. *Automated Spot Weld Inspection in the Automotive Industry*. WCNDT-2004 Proceedings, Vol 10, No 3. (March 2005).

[4] Roman Gr. Maev, Andrei A. Ptchelintsev,John L. Mann , *Transducer built into an electrode* US Patent No 6297467. (2001)

[5] Roman Gr. Maev, Andriy M. Chertov, John M. Paille, Frank J. Ewasyshyn, *Ultrasonic In-Process Monitoring And Feedback Of Resistance Spot Weld Quality*. US Patent No. 706940US1, (2013)

[6] Lui, Anthony, *Development of an Ultrasonic Linear Phased Array System for Real-time Quality Monitoring of Resistance Spot Welds*. Electronic Theses and Dissertations. Paper 4826. (2012)

[7] X sun. *Failure Mechanisms of Advanced Welding Processes*. Woodhead Publishing Limited, (2010).

[8] Masatsune Kondo, Tokujiro Konishi , Koji Nomura & Hiroyuki Kokawa, *Degradation mechanism of electrode tip during alternate resistance spot welding of zinc-coated galvannealed and uncoated steel sheets*, Welding International, 27:10, 770-778, DOI: 10.1080/09507116.2012.708502, (2013)

[9] Hongyan Zhang, Jacek Senkara, *Resistance Welding: Fundamentals and Applications*, (CRC Press, 2005).

[10] Runnemalm, A. and A. Appelgren, *Evaluation of non-destructive testing methods for automatic quality checking of spotwelds*, in SpotLight, report No 13. (2012)

[11] R. Gr. Maev, Accousit Microscopy: Fundamentals and Applications, (Wiley, 2008).

[12]A. M. Chertov, R. G. Maev, and F. M. Severin, “*Acoustic microscopy of internal structure of resistance spot welds*," IEEE Tran. on Ultrasonics, Ferroelectrics, and Frequency Control, vol. 54, no. 8, pp. 1521-1539, (2007).

[13] Waldo J. Perez Regalado, Andriy M. Chertov, Roman Gr. Maev, Valdir Furlanetto, *Integration of the Ultrasonic Real-Time Spot Weld Monitoring System*, 5th Pan American Conference for NDT, (October 2011)

[14] Anthony C. Karloff, *Real-time Expulsion Detection and Characterization in Ultrasound M-scans of the Resistance Spot Welding Process,* Electronic Theses and Dissertations, Paper 4735, (2013).

[15]A. Karloff, A. Chertov, J. Kocimski, P. Kustron, and R. Maev, *New developments for in situ ultrasonic measurement of transient temperature distributions at the tip of a copper resistance spot weld electrode*, in Proc. IEEE Int. Ultrasonics Symp. pp. 1424-1427. (2010)

[16] M. A. Al-Jader, J. D. Cullen, N. Athi and A. I. Al-Shamma'a. *Experimental and computer simulation results of the spot welding process using SORPAS software*. *J. Phys.: Conf. Ser.* 178 012045. doi:10.1088/1742-6596/178/1/012045, (2009)

Chapter 2

Ultrasound Theory and Imaging

Ultrasound is a generic term used to describe any sound waves traveling above the range of human hearing (20 kHz). Ultrasound has a wide range of applications in both medical and industrial fields due to its ability to be used as a detection and characterization tool. This chapter discusses the fundamentals of ultrasound and ultrasound imaging necessary to understand the concepts explored later in this work[1].

2.1 Ultrasound Principles

2.1.1 Sound Propagation

Sound waves are waves that propagate through media due to interactions between the particles. Like all waves they have characteristic parameters such as frequency, amplitude and phase. These parameters, in addition to the properties of a medium, describe how this wave will propagate in space. Like all waves their motion is described though the wave equation, expressed in both it's coupled and decoupled forms by equation 2.1 and 2.2a-c. Here p is the pressure, ρ_0 is the density of the media, u is the particle displacement, c_0 is the speed of sound within the media and t is the time[2].

$$\nabla^2 p - \frac{1}{c_0^2}\frac{\partial^2 p}{\partial t^2} = 0 \tag{2.1}$$

$$\frac{\partial u}{\partial t} = -\frac{1}{\rho_0}\nabla p \tag{2.2a}$$

$$\frac{\partial \rho}{\partial t} = -\rho_0 \nabla \cdot u \tag{2.2b}$$

$$p = c_0^2 \rho \tag{2.2c}$$

2.1.2 Types of Sound Waves

There are multiple ways in which a sound waves can propagate, however for the purposes of this work only two need to be considered. The simplest method of propagation is that of the longitudinal wave, where collision of particles within the medium generates regions of high and low particle density. Additional collisions between the particles allow for the wave to propagate through the medium in the same direction as particle motion. The second type of wave is that of the shear wave. Shear waves are generated when a force is applied to the medium, such that the internal particles are made to oscillate in some direction. The resulting wave propagates within the medium through the bonding forces in a direction tangential to the direction of particle movement. As a result of this propagation method shear waves are often considered to only be supported within solid medium. A diagram depicting these types of motion can be seen in figure 2.1.

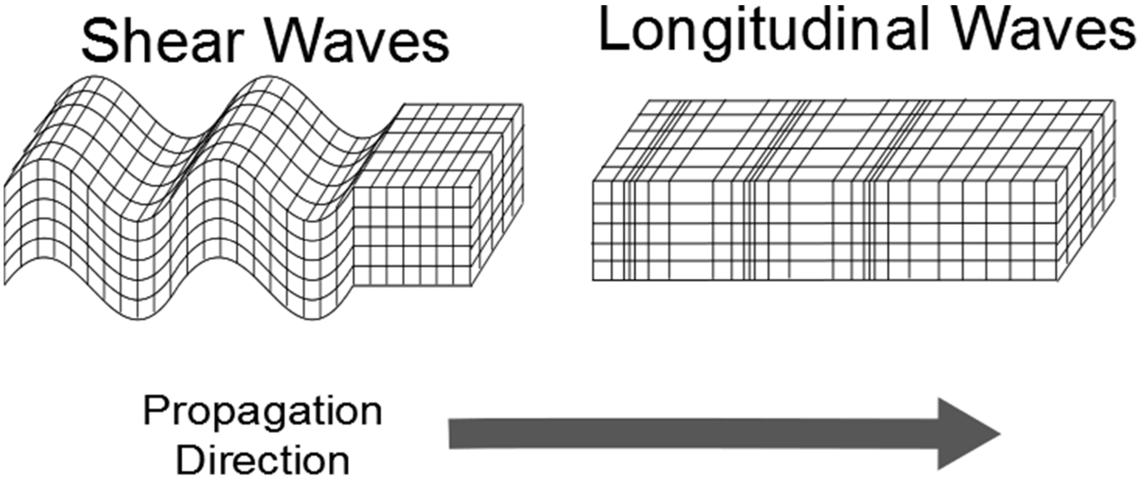

Figure 2.1 - Contrast of the difference between the propagation of shear and longitudinal waves. The particle location in each case is depicted by the intersection of the grid lines. It should be noted that although the particle motion is different in each case the wave's direction of propagation remains unchanged.

Although both waves propagate in differing manner they can be expressed using similar parameters, with the only notable difference occurring due to their varying speed of sound within a material, where shear waves propagate at a lower speed.

The speed of sound within both media can be determined using the elastic constants of the material. The parameters necessary to determine the speed of sound are Poisson's Ratio, μ, Young's Modulus, E, and the density of the media ρ. This can be done using equation[1] 2. 3 and 2.4 for the longitudinal and shear velocity respectively.

$$c_l = \sqrt{\frac{E(1-\mu)}{\rho(1+\mu)(1-2\mu)}} \qquad 2.3$$

$$c_S = \sqrt{\frac{E}{2\rho(1+\mu)}} \qquad 2.4$$

2.1.3 Refraction, Reflection and Transmission

For waves incident upon a boundary, the principles that govern the wave must continue to hold, most notably its continuity and the total energy of the wave across the boundary. In order for these principles to hold the wave must undergo a change in its propagation direction and its amplitude. To determine the resulting change in direction, Snell's law is implemented. This well-known equation describes the change in the waves propagation direction by a ratio of the sines of the incident and transmitted waves angle, θ, with respect to the speed of sounds, c, as given by equation 2.5.

$$\frac{\sin\theta_1}{c_1} = \frac{\sin\theta_2}{c_2} \qquad 2.5$$

In addition to this change in the propagation angle of the wave, the amplitude of the wave also undergoes a change described by the transmission and reflection coefficient. These coefficients express the amount of the wave's amplitude and intensity that is reflected or transmitted at the boundary. This coefficient is related to the degree with which the impedances (equation 2.6) of the media differ. The impedance of a medium, Z, is a parameter that couples the speed of a wave in the medium, c_0, with the density of the medium, ρ_0.

$$Z = \rho_0 c_0 \tag{2.6}$$

The transmission (T) and reflection (R) intensity of the wave at the boundary can be described by the magnitude of its velocity, pressure and intensity, relative to that of the incident wave. In most instances the intensity or pressure coefficients are chosen, as most ultrasound detection techniques are pressure based. The other coefficients can be found through simple relations given in equations 2.7-2.10 below, with the corresponding subscripts for pressure (p), Intensity (I) and velocity (u) used.

$$T_I = T_p T_u \tag{2.7}$$

$$R_I = R_p^2 = R_u^2 \tag{2.8}$$

$$T_p = \frac{Z_1}{Z_2} T_u \tag{2.9}$$

$$R_p + 1 = T_p \tag{2.10}$$

The most basic case of reflection is that of a wave normally incident on the boundary between two media. In this case the coefficients are expressible as a simple ratio of impedances, given by equation 2.11 and 2.12 below. These relations also allow for good approximation in cases of low angles of incidence.

$$R_p = \frac{Z_1 - Z_2}{Z_1 + Z_2} \tag{2.11}$$

$$T_p = \frac{2Z_2}{Z_1 + Z_2} \tag{2.12}$$

In order to deal with a wave incident at an angle, additional considerations must be addressed, mainly the fact that waves incident at angles can excite both shear and longitudinal waves within the media, a phenomena known as mode conversion. In all cases the waves propagate according to the underlying equations and changes in propagation direction occur according to Snell's law. Due to the variety of waves and the fact that not all media support the propagation of shear waves, there are a wide number of situations that can occur. These situations have been investigated mathematically[3] however, a full consideration is not needed in most cases.

In this thesis the primary source of mode conversion is the presence of the copper water boundary in the system. For this reason a wave incident from a liquid media and propagating into a solid must be considered. In order to determine the reflection and transmission coefficients the densities of the media and speed of sound for each type of wave must be known. In addition, the impedance of the media is adjusted to account for angular propagation. This results in an intensity transmission and reflection coefficient described by equations[4] 2.13-2.15, where the angles are taken with respect to those in figure 2.2. Plots of the transmission coefficients corresponding to the water-copper boundary can be seen in figure 2.3. There are two regions of note, mainly the region of low incidence angle, and the region after which the critical angle is encountered, when only shear waves are transmitted into the media. In most system, due to the differing speed of sound between shear and longitudinal waves effort is made to allow for the transmission of only a single type of wave into the media. In these cases other modes of propagation are ignored.

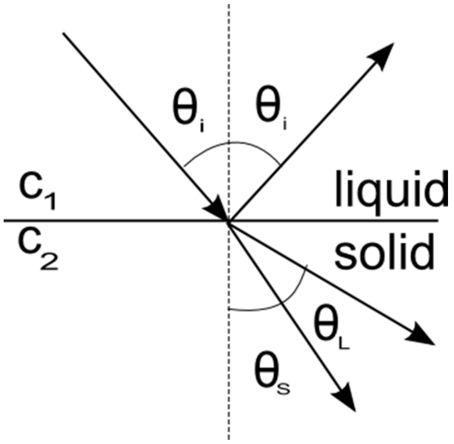

Figure 2.2 – A graphical representation of the direction of wave propagation as it passed through and is reflected from a boundary. Due to mode conversion a ray incident at angle θ_i can produce both a longitudinal and shear wave propagating at angles θ_L and θ_s respectively.

$$R = \frac{Z_2 - Z_1}{Z_2 + Z_1} \tag{2.13}$$

$$T_L = \frac{\rho_1}{\rho_2}\frac{2Z_L\cos(2\theta_s)}{Z_2 + Z_1} \tag{2.14}$$

$$T_s = \frac{\rho_1}{\rho_2}\frac{2Z_s\cos(2\theta_s)}{Z_2 + Z_1} \tag{2.15}$$

$$Z_1 = \frac{\rho_1 v}{\cos\theta_i},\ Z_2 = Z_L\cos^2(2\theta_s) + Z_s\sin^2(2\theta_s),\ Z_L = \frac{\rho_2 v_L}{\cos\theta_L}$$

$$Z_s = \frac{\rho_2 v_s}{\cos\theta_s}$$

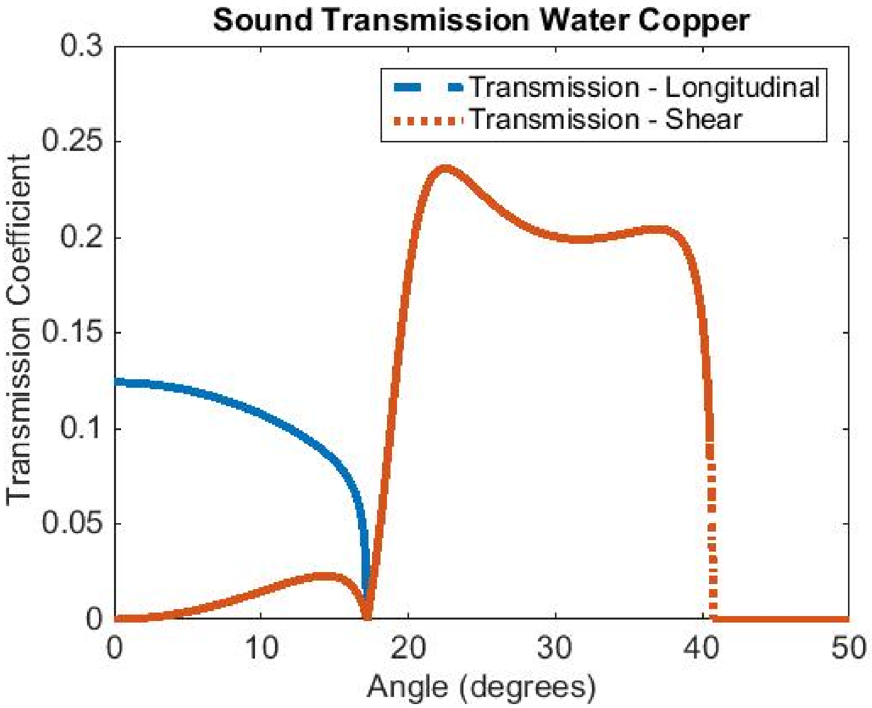

Figure 2.3 - A plot of the transmission coefficients and mode conversion between water and copper for shear and longitudinal waves. In order to reduce mode conversion angles of less than 17° should be employed.

2.1.4 Attenuation of Sound Waves

During propagation through a medium a wave undergoes a variety of interactions within the medium. These interactions generate a loss of the wave's amplitude due to scattering and absorption. Scattering is caused mainly due to the interaction of propagating waves with the grain structure of the medium. At these grain boundaries a high impedance mismatch exists, causing reflections of ultrasound waves. Depending on the size of the grains, these reflections can have a significant effect on the propagation amplitude and direction of the wave, causing losses to occur. Absorption occurs due to the thermal interactions within the medium converting sound to other forms of energy. These losses are often grouped together into a term known as attenuation. The attenuation of a medium is best characterized by the use of an exponential decay. In this case, as the wave propagates through a medium its amplitude A is related[1] to the initial amplitude of the wave A_0, an attenuation factor α (cm^{-1}) and the distance of propagation d in units of cm.

$$A = A_0 * \mathrm{e}^{-\alpha \mathrm{d}} \tag{2.16}$$

As imaging commonly relies on the use of broad frequency ranges, the frequency dependence of attenuation must be considered. In this case the attenuation within a media is best described by a power law attenuation factor, whereby the attenuation coefficient α is expressed in terms of the frequency of the ultrasound wave, ω, and a power exponent factor[1] y.

$$\alpha = \alpha_0 \omega^y \tag{2.17}$$

This power law attenuation results in an uneven attenuation and a loss in resolution as the wave propagates and higher frequencies undergo greater attenuation.

2.1.5 Intensity and the decibel scale

When imaging multiple media, a wide variation in the reflection amplitude of the wave may be present, meaning that imaging often occurs at a wide range of amplitudes. For this reason it is common to express the ultrasound signal on a decibel scale. As ultrasound is measured on a pressure scale the intensity level, L, in decibels can be calculated by relating the amplitude of a wave, A, to a reference amplitude A_0 through equation 2.18. The most common points of reference in the decibel scale are the -6dB and -12dB points, corresponding to the loss of 50% and 90% of the compared amplitude.

$$L = 20\mathrm{dB} * \log_{10} \frac{A}{A_0} \tag{2.18}$$

2.2 Principles of Ultrasound Imaging

Ultrasound imaging like all wave based imaging modalities relies on the principle that a wave undergoes varying changes as it propagates through a medium. By examining those changes, properties of the system can be determined. In ultrasound imaging two imaging modalities are primarily used, notably reflection and transmission based imaging. In order to generate ultrasound waves the use of a transducer is employed to convert electrical impulses to acoustic impulses.

In transmission based imaging waves are sent through the medium to a secondary transducer. This yields only information about the loss in signal and relies on comparison to a reference sample or samples acquired at other spatial or temporal locations for assessment. Although this modality has been previously researched for this work by others[5] it was rejected in favor of reflection imaging, and will thusly not be considered further.

Reflection images are based upon the use of a single transducer that acts as both the transmitter and receiver of ultrasound waves. In this imaging modality a short impulse is sent into the system and the reflections generated from the medium are analyzed in order to allow for the determination of the medium properties. The basics of this process can be seen in figure 2.4, where an amplitude scan or A-scan allows for the determination of the amplitude and time between received reflections. If the speed of sound is known this allows for the determination of an approximate depth at which the reflector is present.

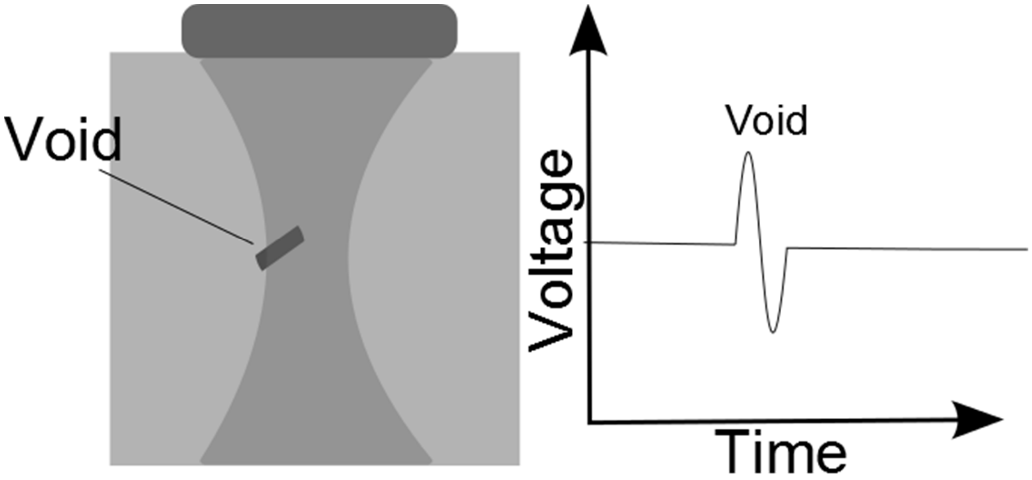

Figure 2.4 - An example of a B-Scan on a media with a void present, any object or boundary within the emitted ultrasound field(left) having its reflections detected and displayed in the resulting image(right).

Although the A-scan allows for the acquisition of information in the direction of wave propagation it is often desirable to acquire information in more than one dimension. In order to do this multiple A-scans can be acquired at differing spatial or temporal locations by translating or rotating the transducer. By representing these scans as an image and correlating amplitude to brightness a B-scan is generated (figure 2.5). As the B-scan terminology can be used for many imaging modalities, within this work it shall be reserved for describing spatially varying images. The moving scan (M-scan) imaging modality will be used to describe B-scans whose frames are acquired at different temporal windows.

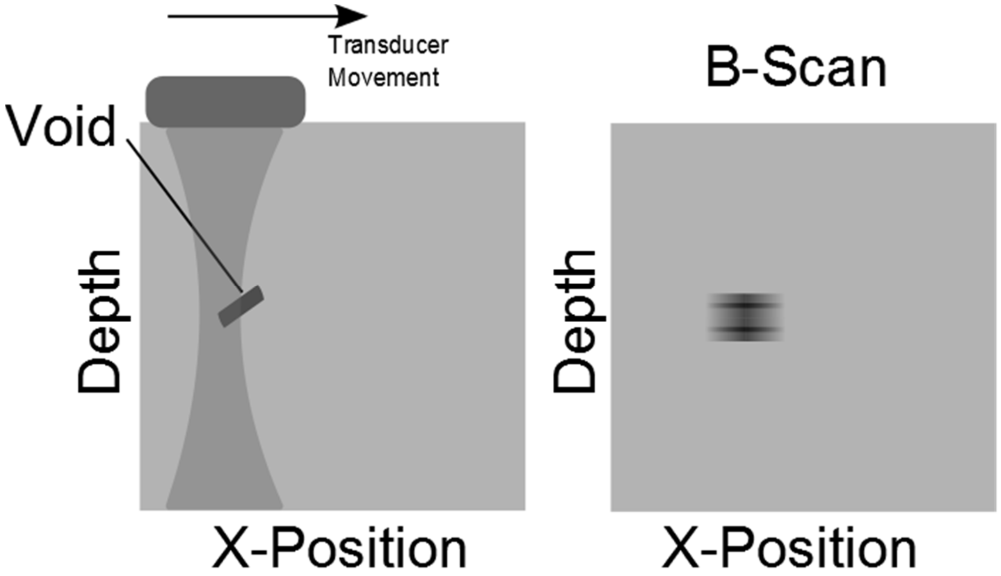

Figure 2.5 - An example acquisition of a B-scan. An A-scan is created by acquiring ultrasound data at multiple scan locations and creating a figure corresponding to the spatial or temporal locations at which these scans are acquired.

All imaging modalities rely on the determination of the properties of the system, but in most cases the introduction of undesired image artifacts occurs due to noise in the system. One of the most common sources of error in ultrasound imaging is due to the fact that the receiver and source of ultrasound do not transmit ideal waves for imaging purposes. As the wave propagates, any objects which do not completely block its path act as additional sources of reflection. This means that for waves with large spatial distributions many reflections result from objects outside of the desired imaging region. In order to prevent this, a transducer must be chosen such that the emitted fields allow for coherent images to be acquired.

2.3 Transducer Selection

During transducer selection the primary parameters that control the imaging process are the size, shape, frequency and pulse duration or bandwidth of the transducer. The frequency of a transducer is the primary factor in determining its resolution. During ultrasound imaging the fields emitted from a transducer result in distinct interference patterns in space. By controlling these interference patterns in such a way that the amplitude is minimized outside of the imaging region it is possible to generate high quality images. The design of an ultrasound probe is often done to allow for a needed resolution to be obtained, while not incurring unnecessary burdens that result from very high resolution systems.

In order to control the fields that are emitted from a transducer the size, shape and frequency of the transducer can be modified. For the purpose of imaging the emitted field of a transducer is separated into two distinct regions, the near field and the far field. In the near field constructive and destructive interference result in a widely varying intensity, with regions of null intensity, while in the far field the intensity decrease proportionally to the distance. These field patterns are characterized in figure[7] 2.6 below.

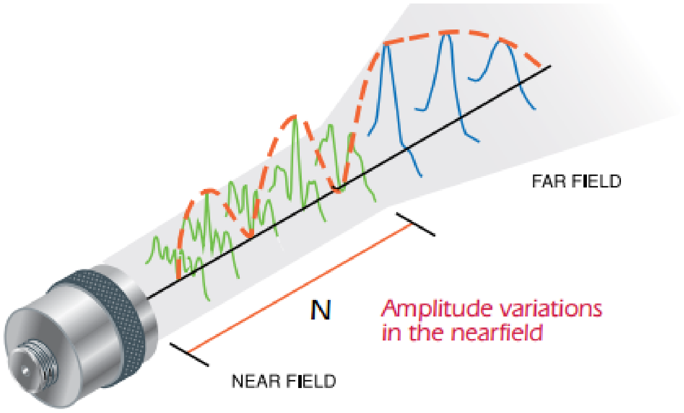

Figure 2.6 - The stark difference between the near and far field emission of a transducer. As is seen, the near field has inherent oscillations in both spatial directions, while the far field is expressed with a far more constant decay of the wave's amplitude

Due to the variability of the wave in the near field, this region is often undesirable for imaging purposes, as any defects can be missed during examination. As the amplitude is constantly decaying in the far field the last maximum occurs at the boundary between the two. This boundary is referred to as the natural focus of the transducer due to its superior imaging characteristics. The location of this focal point can be found using the near field equation[7], where the near field distance N is proportional to the diameter of the transducer D and its wavelength within the chosen imaging medium λ. This allows for the calculation of the required transducer size for a given imaging situation. In cases where multiple media are present the near field is often modified using the small angle approximation. In this case the diameter can be found using the depth of each media and their corresponding wavelengths.

$$N = \frac{D^2}{4\lambda} \tag{2.19}$$

$$d_1\lambda_1 + d_2\lambda_2 = \frac{D^2}{4} \tag{2.20}$$

By changing the shape of the transducer or employing an ultrasonic lens this focal distance can be decreased by altering the interference pattern. Although this allows for higher resolution at the focal point, the more rapid convergence and divergence of the spatial distribution results in a decrease in the focal length of the system, reducing the range of depth over which the beam remains focused and imaging can occur.

In order to quantify the resolution of the system a common point of measure is the -6dB. This point is chosen due to the fact that it corresponds to the full width half max of the pressure emitted and describes the spatial resolution of the system. The -20db location of the system is also given in some situations as additional reference.

The temporal resolution of a transducer is determined by the pulse duration, defined as the period of time over which the wave’s enveloped amplitude decays, again specified using the -6db measure of the wave. The pulse duration of a probe is primarily influenced by the design process and methods used to manufacture the probe.

2.4 Principle of Superposition and Phased Array Imaging

One of the primary problems with traditional imaging modalities is that the time required to translate or rotate the transducer makes imaging some processes impossible or impractical. In order to overcome this the use of phased array imaging is employed.

Phased array imaging makes use of Huygens' principle of superposition, which states that any source of ultrasound can be broken down into individual point sources of ultrasound, as long as the point sources are separated by less than the Nyquist limit of the wave[8]. Phased arrays make use of the principle by dividing an ultrasound transducer into sub elements. By choosing the active elements it is possible to vary the size of the active emitter and it's corresponding field patterns. In addition to this it is common to employ electronic delays to each element to further manipulate the emitted fields, as shown in figure 2.7. These delays, known as focal laws, are chosen such that the waves emitted from each element arrive in phase with each other and are directly proportional to the difference in time of flight between each element and the focal point.

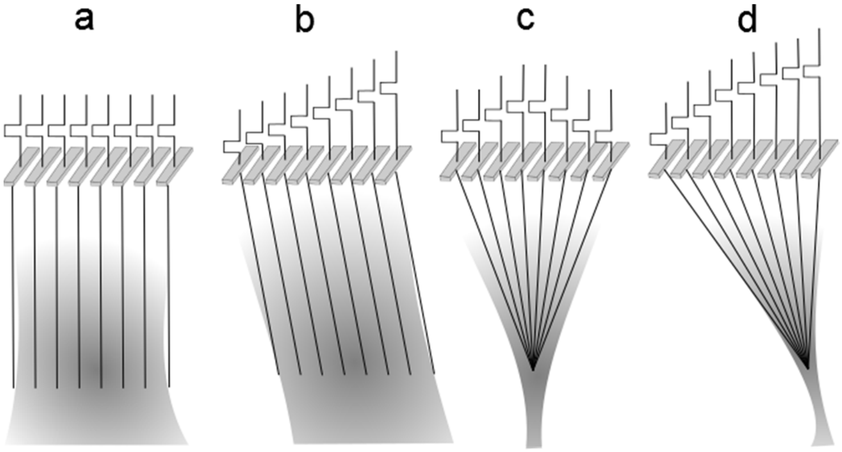

Figure 2.7 - A depiction of the electronic delays and emission fields of a phased array probe for electronic steering (a and b) and electronic focusing (c and d) with and without steering applied. It should be noted that near fields and far field variations exist for all cases.

During the design process the array parameters must be considered to allow for optimal imaging. When sizing the array, the number of array elements, pitch (spacing between the center of the elements) and the inter element spacing (size of the cuts used to section the transducer into sub elements) can be varied to allow for a variety of imaging situations. These parameters, summarized in figure 2.8 below can be modified to optimize the array for specific applications.

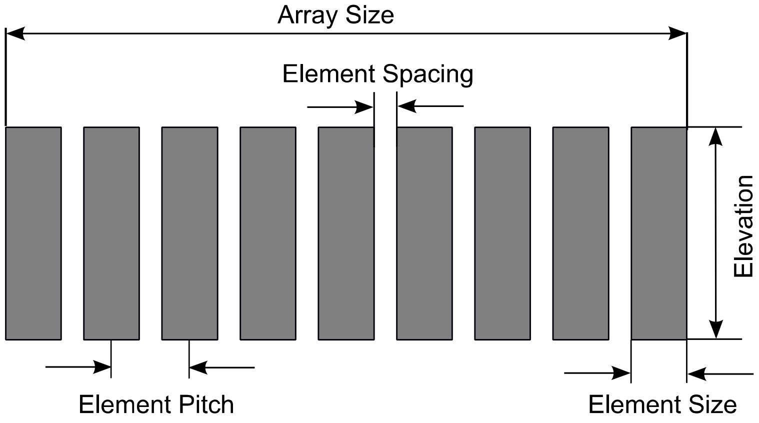

Figure 2.8 – A diagram depicting the various parameters of the phased array. These properties can be modified to maximize imaging abilities for specific situations.

As phased arrays rely on the use of superposition to optimally focus, the array elements must be chosen such that the Nyquist sampling criteria is met, mainly the elements are sized such that they are less than half the size of the emitted sound wavelength. If this condition is not satisfied imaging artifacts can occur due to the presence of additional lobes in the emitted fields.

2.5 Ultrasound Acquisition System

In order to acquire ultrasound data an ultrasound acquisition system must be used. These systems often consist of multiple components and subsystems depending on the application they are to be used for. In the simplest case an ultrasound system consists of a pulsar and receiver board along with control electronics and a processing system.

Pulsar boards consist of one or more pulse generator units. Simple pulsar boards allow for the use or a unipolar or bipolar impulse to drive the ultrasound transducer. Although more complex systems allow for arbitrary waveforms to be generated they are rarely used in industrial applications due to their lower energy limit. Pulsar boards allow for the control of the input pulse waveform at selected voltages and emission windows. As the input pulse controls the emitted ultrasound wave the board should be capable of generating impulses of between one quarter and one half wavelength of the transducer frequency, as these are the typical emission lengths chosen to optimize signal quality. If phased array imaging is to be used the use of multiple pulsar boards can be employed alongside delay electronics to vary emission patterns.

In order to acquire ultrasound signal the use of an ADC (analogue digital converter) is coupled with amplification electronics. Any pressure incident on the transducer will cause a voltage to be present across the ADC channel. Amplification is performed before the data is sampled in order to allow for acceptable voltage levels to be present for conversion. The two most important parameters of the ADC board are its sampling rate and digitization ability. In order to acquire the signal, samples must be taken at a chosen sampling rate, typically 50-100MHZ for phased array systems. For each data point the amplitude is discretized into an amplitude value in bits. For any ultrasound system the sampling rate must be chosen such that both the desired frequency can be can be expressed and the amplitude is not saturated. Amplifiers must be chosen such that the produced noise does not affect signal quality.

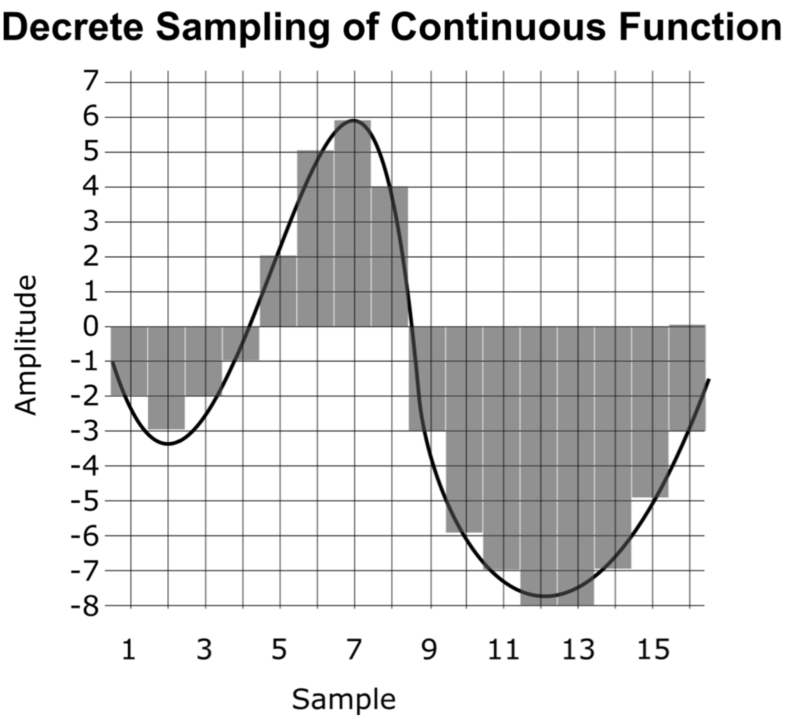

Figure 2.9 - A depiction of the sampling of a continuous waveform at discrete amplitudes and time values, depicted using points and lines respectively. Improper discretization of both the frequency and amplitude can result in large errors when reconstruction is attempted.

These two boards are coupled together with electronics that allow for rapid transfer between the emission and reception boards, allowing a transducer that has been used to emit the signal to sample immediately after. In order to reduce the cost of the system it is common to use multiplexers to select active elements. This allows for an arbitrary choice of elements for emission and reception of ultrasound data as long as the number of chosen elements does not exceed the capabilities of the system.

The rest of the ultrasound system is often less well defined, but contains the electronics necessary for the storage and processing of the received data, as well as a communications board to transfer data.

2.6 Full Matrix Capture and the Total Focusing Method

Although phased array imaging is a commonly employed technique, recent advances in both the electronics that control the transducer and the systems that process the received data have allowed for the implementation of more powerful imaging techniques. One of these advanced techniques is known as full matrix capture and the total focusing method.

This method relies on the use of Huygens' principle in its most decomposed form. In this case each element of a phased array is treated as a point source of ultrasound. By transmitting with a single element and receiving the reflected signal using all elements the response of the system to the point source input can be found. Repeating this for all elements within an array allows for the acquisition of full matrix data. Using this data and Huygens' principle the signal of any focal pattern can be created by superimposing the responses with the corresponding offsets used to create the focal pattern.

One of the most powerful techniques using this principle is that of the total focusing method. This method, often referred to as the gold standard in imaging[9] uses the full matrix data to focus the array to every point in the imaging space. In order to do this the delays to each point within the media are calculated with respect to each transmit receive pair. By averaging the ultrasound data corresponding to each point for all transmit receive pairs an image can be created. Although this method has distinct advantages in terms of resolution its primary deficit is the fact that the amplitude of the signal that is transmitted into the media is reduced. Although averaging allows for a significant gain in the SNR of the image, the net effect results in a loss of SNR that is approximately $^{1}/_{\sqrt{N}}$, where N is the number of elements in the array. As this noise decrease is only present on stochastic or random noise this is not an issue with most modern acquisition systems.

Full matrix capture has the advantage of a much simpler electronic implementation than traditional ultrasound systems due to the need for only a single transmitter[10], but often requires a significant increase in the computation complexity and scan time depending on the probe's dimensionality. Although a real time implementation has been shown to be possible using modern processors or general purpose graphics processing units (GPGPU) implementations[11] the frame rate required within this work limit it to post processing.

2.7 K-Space Pseudo Spectral Modelling of Ultrasound

Although ultrasonic principles provide a good starting point in the design and analysis of an imaging systems, they often work only in simple cases. Due to the high cost of ultrasound probes, performing experimental validation of multiple designs is often impractical. For this reason the use of computational models has become common in the analysis and design of systems. These models have distinct advantages as they allow for testing of a wide multitude of situations and allow for direct visualization of the amplitude fields.

All computational models rely on the fact that the system in question can be expressed using a combination of underlying equations and mathematical techniques. When using these computational techniques it is important to know the limitations of the program you are using in terms of both the physical phenomena it can express and the limitations of the mathematics used to do so.

For the most part, models rely on breaking down a continuous media into a finite set of spatial points. In the case of wave motion this grid is used to express the wave's spatial properties such as amplitude and frequency. Depending on the choice of techniques used the amount of points needed to express the wave properly can be determined.

Most computational models rely on mathematical expressions such as finite difference models. In this system the propagation of a wave is expressed through the calculation of spatial derivatives. In these cases a large number of grid points are needed within any medium to express the wave's motion and parameters without introducing errors. The use of the k-space method attempts to relax this through the use of the Fourier expansion to express the wave. This has the advantage of needing only two grid points per wavelength in order to express a wave within a single medium[12]. This model also has the computational advantage in that the entire grid is used to express the wave's functional form, as opposed to the select number of grid points in finite difference models. This advantage is noted below, where a function f is expressed using varying methods.

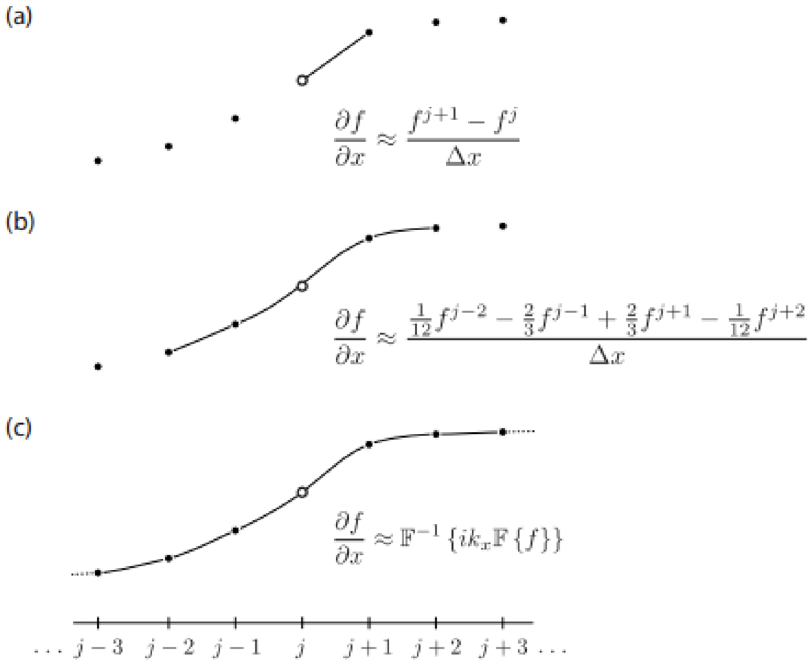

Figure 2.10 - A comparison of differing calculation techniques for spatial gradients using a) first order forward difference, b) Fourth order central difference, c) Fourier collocation spectral method [12].

This modelling method was employed in this research through the use of the k-wave toolbox for MATLAB[13]. In this toolbox the wave is expressed using the fast Fourier transform in the spatial domain, with its temporal evolution expressed using a forward difference time model. Although this technique has been published [14] for use in cases of biological tissues it is important to consider the limitations imposed when modelling cases of higher discontinuity, such as those present in this work.

Like many models this toolbox has no theoretical limitations, however its use is somewhat limited by the computational hardware available. One of the key limitations of this technique is its ability to model large impedance mismatches within the media. This limitation occurs due to the fact that the wave is expressed as a Fourier expansion, meaning that large discontinuities can suffer from the Gibbs phenomena (figure 2.11). The Gibbs phenomena simply defines that there is a limit that prevents proper discretization of effects at the edge. This phenomena is influenced mainly by the number of terms in a Fourier expansion, and does not affect points that are not on the boundary. Although this does not pose a limitation in all cases, in order to prevent this effect from invalidating the results of the simulation care must be taken in the selection of the grid and time step to minimize its influence. Although some recommendations are given within the toolbox in order to aid in the choice of the time step used, the choice of grid spacing is best found through a gradual reduction in grid spacing until any artifacts or differences occurring are eliminated.

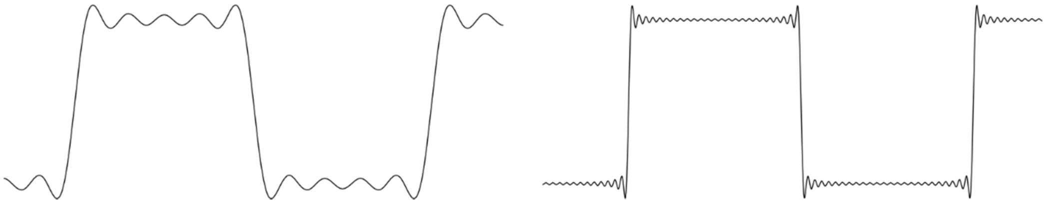

Figure 2.11 - An example of Gibbs ringing artifacts caused by high discontinuities within the media. As can be seen, only the decay rate of the amplitude is modified through the increase of the spectral sampling with the initial overshot remaining constant.

Although these limitations did pose some difficulty in the initial stages of this work, they did not impact the results in any critical manner with the proper choice of computational grids. Although these grid sizes do increase the computational model complexity the required time is greatly reduced due to the fact that this model allows for the use of a GPGPU to accelerate computations [14]. This and the fact that this toolbox is available as a free plugin for MATLAB were the primary reasons for its selection over other simulation programs.

In addition to these effects, a 2D model was implemented in this study. Although this simplification is common in numerical models it presents a fundamental issue in ultrasound. This occurs due to the fact that in a 2D ultrasound system the wave has no physical equivalent (such as plane waves in 1D models). In order to allow for simulations the wave source must be assumed infinite along the 3rd dimension or axial symmetry must be employed. As no symmetry exists within the system in this thesis the third dimension is assumed infinite. This will cause a tailing of the wave, whereby a constant finite amplitude is added onto the tail end of the wave as a result of this assumption.

References

[1] Krautkramer, J. and Krautkramer, H. *Ultrasonic Testing of Materials*. 2nd ed. New York: Springer-Verlag. (1977).

[2] M. F. Insana and D. G. Brown. *Acoustic scattering theory applied to soft biological tissues, in Ultrasonics Scattering in Biological Tissue*. K. K. Shung and G. A. Thieme, eds., pp. 75– 124, Boca Raton: CRC Press. (1993).

[3] Bertram Alexander Auld. *Acoustic fields and waves in solids*, Volume 2. (R.E. Krieger, 1990).

[4] Joseph L. Rose. *Ultrasonic Waves in Solid Media*. (Cambridge University Press. 2004).

[5] Andriy M. Chertov and Roman Gr. Maev. *A One-Dimensional Numerical Model of Acoustic Wave Propagation in a Multilayered Structure of a Resistance Spot Weld*. IEEE Transactions on Ultrasonics, Ferroelectrics, and Frequency Control, vol. 52, no. 10. (2005).

[6] B. E. Treeby and B. T. Cox. *Modeling power law absorption and dispersion for acoustic propagation using the fractional Laplacian*. J. Acoust. Soc. Am., Vol. 127, No. 5. (2010).

[7] *Ultrasonic Transducers Technical Notes*. (1st ed.). Retrieved from: https://www.olympus-ims.com/data/File/panametrics/UT-technotes.en.pdf, (2006).

[8] MV. Klein, TE. Furtak, *Optics*. (John Wiley & Sons, New York, 1986).

[9] O. Oralkan, A. Sanh Ergun, JA. Johnson, M. Karaman, and U. Demirci. *Capacitive micromachined ultrasonic transducers: next generation array for acoustic imaging*, IEEE transactions on ultrasonics, ferroelectronics and frequency control, 49(11):1596–1610, (2002).

[10] C. Holmes, B. Drinkwater, and P. Wilcox, *Post-processing of the full matrix of ultrasonic transmit–receive array data for non-destructive evaluation*, NDT & E International, vol. 38, no. 8, pp. 701-711, (2005).

[11] Mark Sutcliffe, Miles Weston, Ben Dutton and Ian Cooper. *Real-time full matrix capture with auto-focusing of known geometry through dual layered media*. NDT 2012, BINDT, (September ,2012).

[12] Bradley Treeby, Ben Cox, and Jiri Jaros. *k-Wave A MATLAB toolbox for the time domain simulation of acoustic wave fields User Manual*, New York: Springer-Verlag, (2012).

[13] B. E. Treeby and B. T. Cox, *k-Wave: MATLAB toolbox for the simulation and reconstruction of photoacoustic wave-fields*, *J. Biomed. Opt.,*vol. 15, no. 2, p. 021314, (2010)

[14] B. T. Cox, S. Kara, S. R. Arridge, and P. C. Beard. *k-space propagation models for acoustically heterogeneous media: Application to biomedical photoacoustics*. J. Acoust. Soc. Am., vol. 121, no. 6, pp. 3453-3464, (2007).

Chapter 3

Experimental Setup and Design

During the initial stages of this research issues were found with the design of the system that prevented optimal imaging. As a result of these issues investigation was performed to determine the cause and provide a solution. As a result of this investigation a complete redesign of the system was undertaken to improve image quality and optimize the ability to implement the design. This chapter covers the previous system, the redesign process and the imaging constraints of the current system.

3.1 Current State of Art

In the original design of the RIWA system an array implementation was desired, however, hardware and computational requirements of such a system made implementation impossible at the time. Although an array based implementation was later investigated using through transmission imaging[1], analysis and interpretation of the resulting data proved difficult due to limited information that this acquisition technique provides. Eventually a reflection based imaging system was developed and showed good success[2]. This system allowed for the acquisition of reflection based images along a single cross section of the weld and was used as the basis for this work.

The previous system was composed of a 24 element linear array with specifications given in table 3.1. This probe was housed inside of a large copper housing, seen in figure[1] 3.1, with an inlet and outlet drilled into the sides of the housing to provide cooling and prevent overheating. In order to allow for the computation of focal laws (the delays necessary for focusing) the cap's internal surface was machined flat. To create and a two boundary system, steel was ignored and instead replaced by an equal thickness of copper. Although this system allowed for the acquisition of ultrasound data in the desired manner, many problems were found with this prototype design after its construction that made its use difficult in a laboratory setting and potentially impossible in an industrial one.

Frequency	10 MHz
Number of Elements	24
Element Size	0.15 mm
Inter Element Spacing	0.05 mm
Elevation	4 mm
Pulse Duration	Minimal

Table 3.1 - The Specifications of the previous phased array design

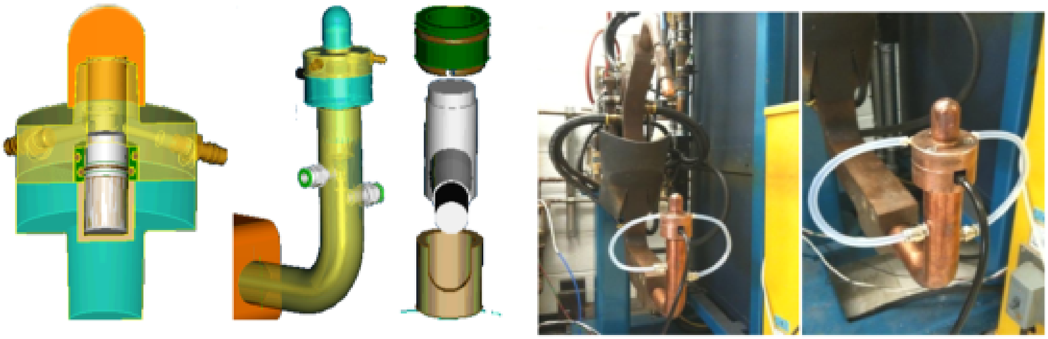

Figure 3.1 - The housing of the previous probe was designed to allow for water to be supplied via external channels. A small plastic insert was used to electrically separate the transducer from external currents, as well as prevent leaks.

Due to the geometry of the water inlet and outlet tubes, as well as the placement of the transducer small pockets of air could regularly became trapped within the housing at the probe surface or the top of the copper cap, depending on orientation. These air pockets prevented the transmission of sound and were found to be difficult to eliminate. Although this was an inconvenience in the laboratory the time required to do this would be unacceptable in an industrial environment. The size of the housing and external water tubing also made its use impractical outside of the laboratory settings due to the clearance required in many welding setups.

Aside from practicality concerns, issues with the imaging ability of the system were also raised. One of the primary problems with the imaging system was that the images obtained in non-ideal settings were of such low quality as to be unusable. One of the primary reasons for this was the fact that the imaging process makes use of a dry coupled contact between the copper and steel boundaries. This contact means that sound is only transmitted through the imperfections in both surfaces that come in contact when pressure is applied. Although the transmitted sound is well above the noise level of the current acquisition system the amplitude of this reflection poses a problem due to its proximity to subsequent reflections. When poor transmission occurs these subsequent reflections are often far below the amplitude of the original reflection's tail and make the detection of them difficult without complex processing techniques.

The final issue that was found in the initial design was the size of the probe. As phased array focusing makes use of delay laws to implement focal arrangements similar to that of single element transducers the size of the aperture must be selected to allow for a proper focus to be achieved. By calculating the near field length of the transducer, it was found that a proper focus could not be achieved even when the full array was implemented. This effect can have varying consequences, depending on the system, and was a cause for concern.

In order to determine the effects of the design limitations on the image quality an evaluation of the system was performed. In the past the system's imaging abilities were assessed through the use of steel plates with both holes and slots bored into their surface. Although images obtained of the holes were found to be unusable, the slots allowed for the conclusion that the system was able to differentiate between objects of differing size[2]. This experiment, although important, does not fully quantify the resolution abilities of the system, which are best characterized by the spatial distribution of the waveform within a medium, which directly relates to its response to a point source reflector within the medium. In order to determine this distribution, a 2D model of the system was developed to allow for the direct measurement of the waveform's amplitude under ideal conditions. This model makes use of a 2D setup, shown in figure 3.2, to represent the system. For the purposes of modelling the presence of shear waves, attenuation and the dry coupling of copper and steel were ignored due to the low angle of incidence and the fact that attenuation and dry coupling can vary greatly between copper caps and will have an unpredictable effect on imaging.

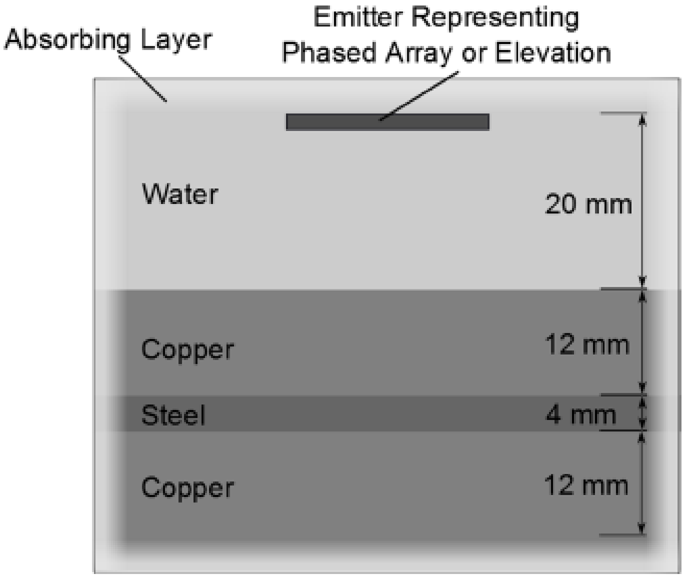

Figure 3.2 - The simulation environment, consisting of the three media within the system. The geometry of the copper cap is ignored for simplification and perfect coupling assumed between each media.

With this in mind simulations were performed for both the focusing direction and the elevation direction. In all simulations performed the time step was chosen according to the grid discretization to guarantee stability of the model and the grid size refined until numerical agreement was reached between step sizes. In order to prevent wraparound effects at the boundaries of the system a perfectly matched layer was added around the grid and its parameters chosen to sufficiently attenuate the wave and prevent reflections.

In order to examine the system's response the square of the pressure field was plotted along both the axial and lateral directions within the desired imaging region. When the focus occurred off center from the probe, the amplitude profile was extracted by tracking the maximum from its origin at the center of the array. These fields, outlined in figure 3.3 were simulated using a 2D acoustic model. As a 3d model is not employed it is important to note that both the elevation and phased profiles contribute to the full spatial profile. As a result of this the design must be chosen such that both phased and elevation profiles allow for imaging to occur within the region of interest.

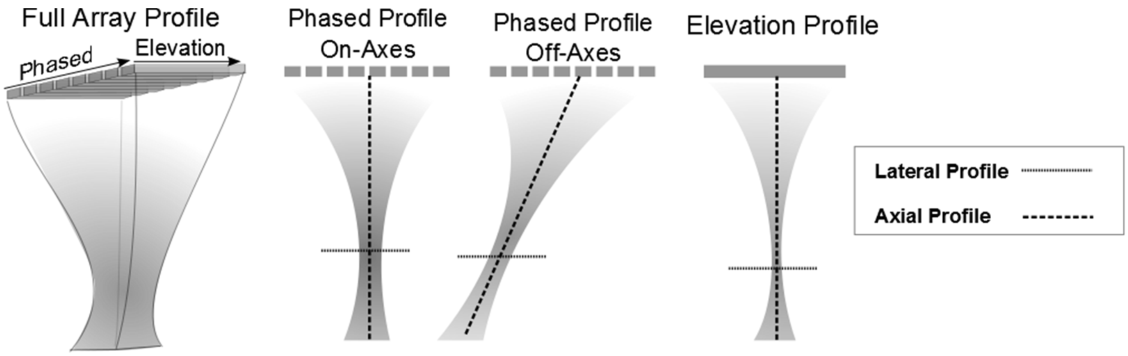

Figure 3.3 – A depiction of the array's emission profile and its varying components.

The first analysis conducted was that of the focus in the elevation direction of the probe. In an ideal situation the probe will be well focused in this direction, such that any analysis can assume that for the region of imaging only a thin cross sectional view of the material is acquired. The results of this simulation, seen in figure 3.4 show that this assumption in difficult to employ in this case. The spatial spread in the elevation direction was found to have a full width half max (FWHM) of 2.6 mm. This indicates that the any image obtained using this system will be composed of features not only along the center, but along a much wider field of view. As the spot weld cap surface ranges from 4.8-8.0 mm in most applications this means that the image quality may be significantly degraded.

Although the spot size was found to be larger than desired, the lack of attenuation within the model means that its spatial distribution as a function of depth can be directly related to its axial profile. The axial profile is indicative of how much amplitude is lost due to spatial broadening of the wavefront. In this case, the loss of 0.7dB along the imaging region indicates that essentially no depth effects need to be considered in focusing. This lack of focus is likely the reason for the inability to detect the holes in the initial experiments.

Although the elevation spot size prevents the use of the cross sectional assumption, estimations of the nugget size may still be possible despite this distortion. In addition the use of lensing structures may also be implemented to correct this. The probes focal spot size in the phased dimension is inherently limited by the total size of the probe, meaning that its resolution must be examined and be found acceptable for imaging to occur. In order to quantify this, a similar simulation was performed, however, as the focal spot size can vary with angle, both an on axes and off axes focus was simulated. For the off axes point a focal spot at -4 mm from the center of the cap surface was simulated to allow for a worst case scenario. The results of these simulations, shown in figure 3.5 and 3.6 were found to show that the probe was capable of imaging with a resolution of 1.80 mm at the FWHM. This indicates that no object smaller than this spot size can be discerned and that any object larger will be blurred out by this distribution. Once again it was found that in both cases the axial amplitude did not vary to a significant degree within the imaging region. Meaning that the entire image can be acquired with a single pass.

With these results in mind, and the inability to modify the existing housing in a way that would allow for industrial implementation a redesign of the system was considered to improve the imaging quality.

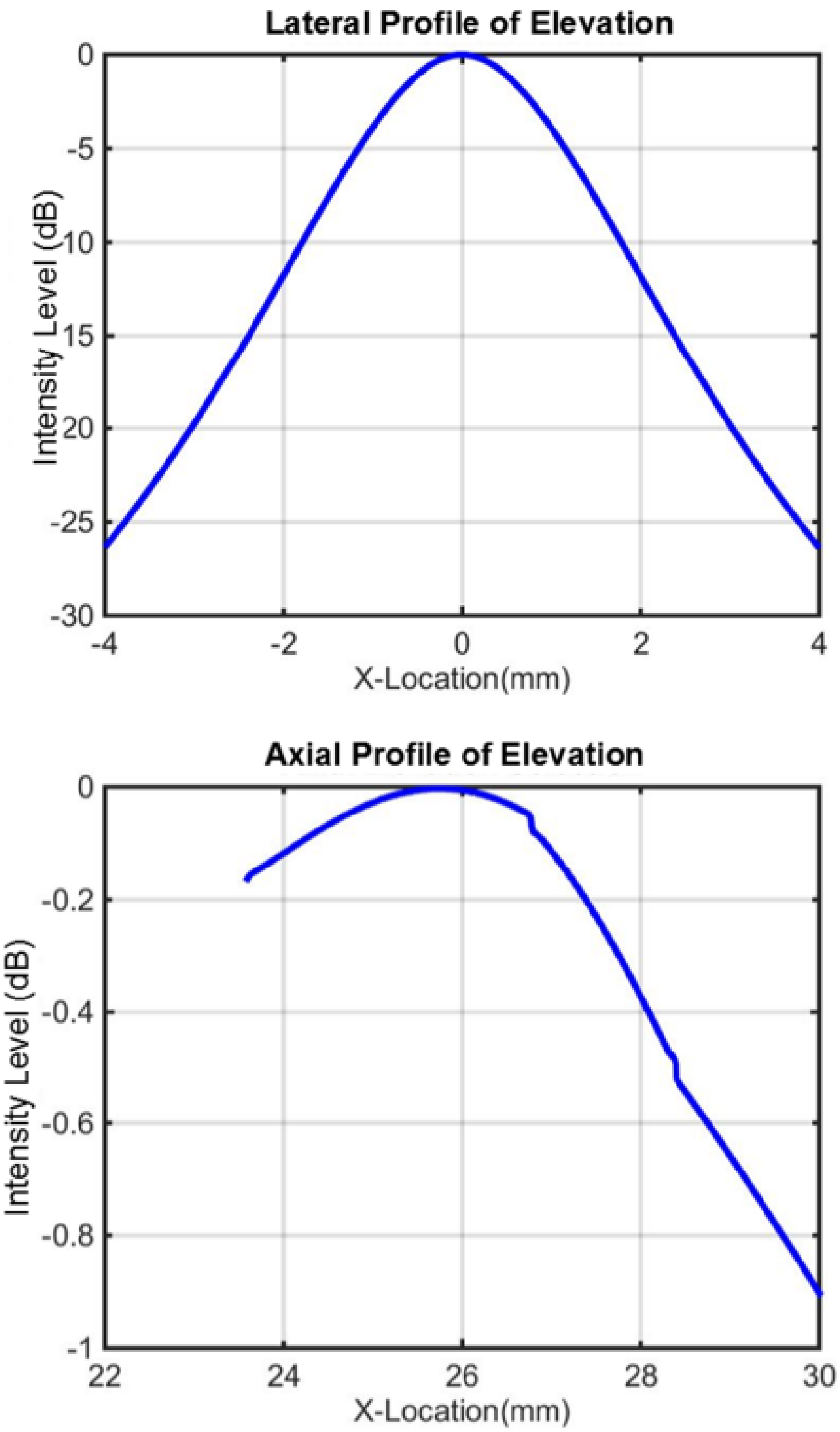

Figure 3.4 - The depiction of the amplitude distributions for the elevation of the previous transducer.

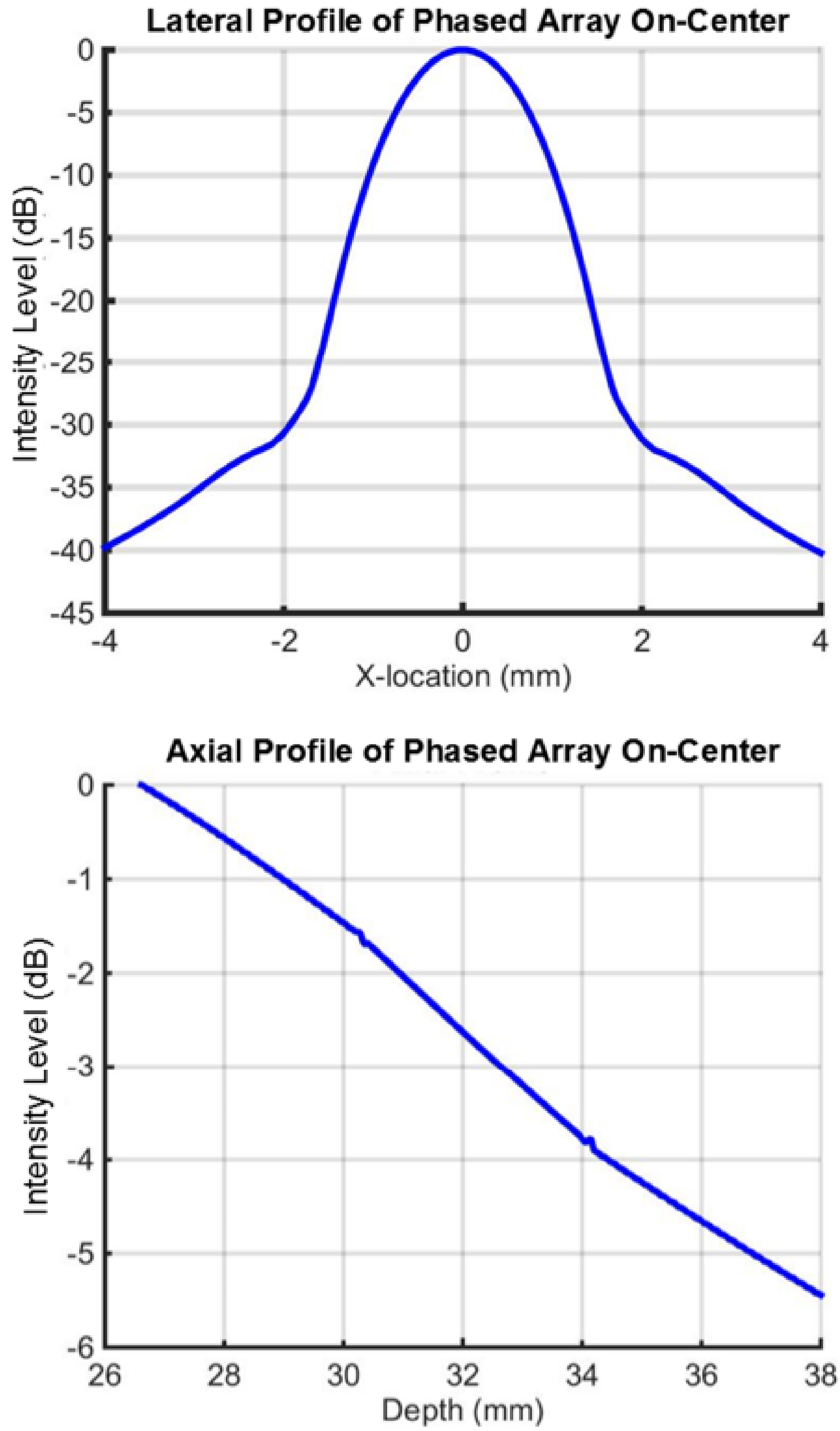

Figure 3.5 - The depiction of the amplitude distributions for an on-center focus using the previous phased array design.

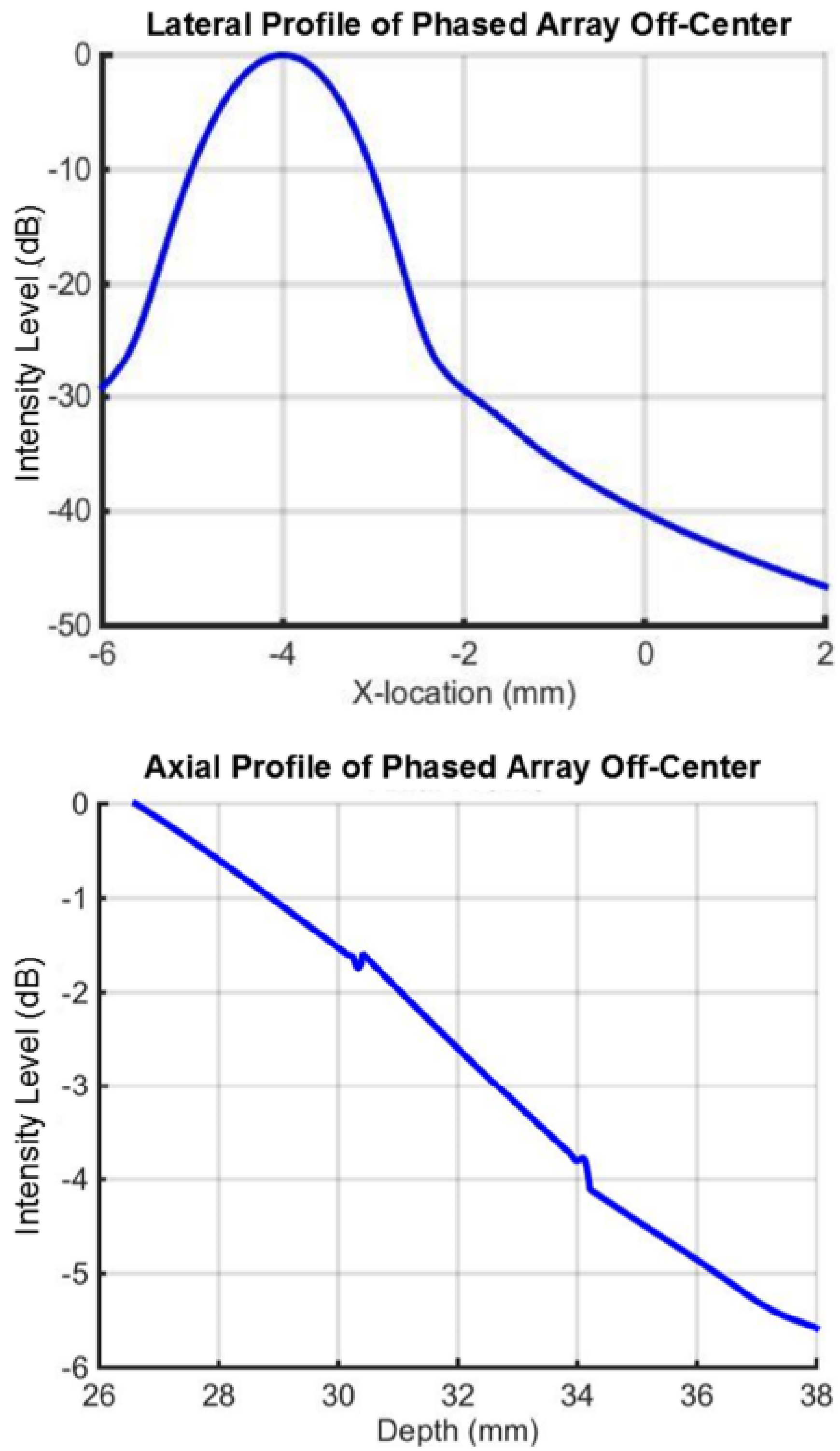

Figure 3.6 - The depiction of the amplitude distributions for an off-center focus using the previous phased array design.

3.2 Restrictions of Imaging System

Redesigning the system posed multiple problems with regard to the constraints placed on the design. In order to allow for testing of the system with existing equipment and minimize integration costs the housing was designed to conform to existing equipment specifications in terms of fittings and electrode caps. It was also decided that the water cooling would be integrated into the electrode to prevent possible damage during operation. Considering that the electrodes are cylindrical in design, the optimal geometric arrangement was to make use of a rectangular transducer housing which allows for the flow of water using the gaps generated by the design, seen in figure 3.7. Due to the mechanical forces used within the spot weld process a maximum diameter of 12.5 mm was set for the cavity to prevent damage to the taper upon which the welding cap sits.

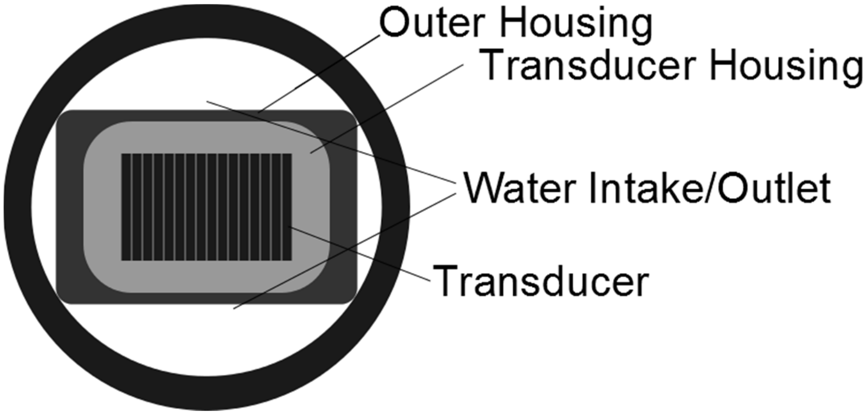

Figure 3.7 - An example of how a rectangular transducer can be used within a circular housing to allow for cooling water to be incorporated into the design

Further limitations were placed upon the design due to the nature of piezoelectric materials. Most piezoelectric compounds cannot sustain high temperatures for extended periods of time. Although high temperature probes do exist, the expense and limitations used in their design proved impractical for the system. As a result of this, adequate cooling must be provided to keep the temperature of the water at the surface of the transducer below 75˚C for extended periods of time.

3.3 Elevation Selection and Lensing

The current analysis makes use of the assumption that imaging occurs along the central slice of the weld. As this was shown not to be the case it was decided that the new system would be designed in such a way as to allow this assumption to hold true. In order to accomplish this a lensing system was needed to properly focus the beam along the axis. In the previous work[2] it was recommended that a spherical lens be employed in the copper cap, as is used in the current single element system. Although it is possible to develop delay laws that allow for focusing to be employed through such a boundary, the angular dependence of the reflections will result in an uneven transmission. Due to this, and the increased difficulty of focusing through a circular boundary it was instead decided that a cylindrical lens would be employed within the copper cap. Although such a lens could be implemented into the transducer itself, this would have fixed the focal length of any system, for this reason the copper was instead used as a lens.

In order to design an optimal lensing effect the ray transfer matrix method[4] was employed. This method is common in optics, but can be adapted for acoustics with relative ease through the substitution of the speed of sound relation for that of the refractive index. As the reference speed cancels in all cases the choice of reference material does not matter using this method. In order to simplify the mathematics and allow for analytic solutions the steel boundary was ignored in the system and was replaced with an equal thickness of copper. Although this will cause a small error in the focal depth this substitution should not result in any significant error due to the similar speeds of sound within the two medium. With this in mind the transfer matrices used with the system, mainly the free space transmission and the transmission at a curved surface, given by equations 3.1 and 3.2 below can be used to determine the optimal lens radius. Here where d is the thickness of the media in which the wave is propagating, c_1 and c_2 are the corresponding speeds of sound and R is the radius of the lens.

$$\begin{bmatrix} 1 & d \\ 0 & 1 \end{bmatrix} \tag{3.1}$$

$$\begin{bmatrix} 1 & 0 \\ \frac{c_2 - c_1}{Rc_1} & \frac{c_2}{c_1} \end{bmatrix} \tag{3.2}$$

When this is implemented the ray transfer matrix of the system becomes that of equation 3.3 below, where x and θ are the position and angle of any incident ray, c is the speed of sound within each medium, d_2 is the thickness of the copper cap and R is the radius of curvature. Due to the fact that the elevation is considered to be a plane wave transmitter for focusing, the angle of each ray can be assumed zero ($\theta_1 = 0$). The final x position of each ray is desired to be the center of the system ($x_1 = 0$), which means that the matrix can be solved with some ease. When this is done it is found that the radius of the lens should be chosen to be 2.26 times the thickness of the copper column.

$$\begin{bmatrix} x_1 \\ \theta_1 \end{bmatrix} = \begin{bmatrix} 1 + \frac{d_2(c_2 - c_1)}{Rc_1} & 0 \\ \frac{c_2 - c_1}{Rc_1} & \frac{c_2}{c_1} \end{bmatrix} \begin{bmatrix} x_2 \\ \theta_2 \end{bmatrix} \tag{3.3}$$

In order to allow for a greater focus to be achieved when steering the beam without a significant increase to the array size it was decided that the transducer would be brought closer to the copper boundary, reducing the water column length to 15 mm. The copper thickness was left untouched due to concerns with overheating that has occurred with the RIWA system in the past.

With these constraints set the primary parameter to be determined was that of the optimal elevation size. Although theoretically the maximum focal ability will be achieved with the largest size possible it must be noted that this will result in a decrease in the focal length of the field. The focal length must be chosen to be of adequate length to account for polishing that occurs to the cap surface after welding and to allow for phased array focusing to occur along the desired focal range. Due to the fact that the focused ray may have an angled trajectory through the medium a longer focal length was desired. With these considerations in mind the desired focus was both narrow and long.

In order to determine the optimal size, varying elevations were simulated. The frequency of the probe was maintained at 10 MHz due to attenuation concerns of the copper. For each of these plots the amplitudes along the axes and at the focal distance were plotted as before. In order to allow for a direct comparison the amplitudes of each profile have been normalized, although it should be noted that the amplitude will increase proportionally with the increased size of the emitter. These plots, seen in figure 3.8 allow for a determination of the focal quality of the system for each arrangement. Considering the size requirements of the system a 5 mm elevation was selected to trade-off between the water inlet/outlet sizes and still allow for a good focus. This choice in elevation allows for an 80% amplitude to be maintained over a region of approximately 10 mm, with a FWHM of 0.9 mm.

As the transducer was to be placed within a copper housing manually it was assumed that some variation in the chosen position of the transducer would occur. Although the water column length has no effect in the ray transfer matrix used to derive the lens radius it will result in an increased or decreased spatial spread of the wave prior to its incidence on the lens. As the derivation assumed that a planar wave was incident upon the surface of the lens it is important to consider the effects these small variations in the transducer placement will cause. In order to do this the simulation process was repeated for a varying water column length. These results were then plotted with a spatial offset to align the focal points of the probes and ease the comparative analysis. These graphs, shown in figure 3.9 reveal that the change in the spatial distribution of the focus for the system is negligible within the chosen 3 mm tolerance in probe position. This indicated that the system should have a very high tolerance to any changes that result from the assembly process.

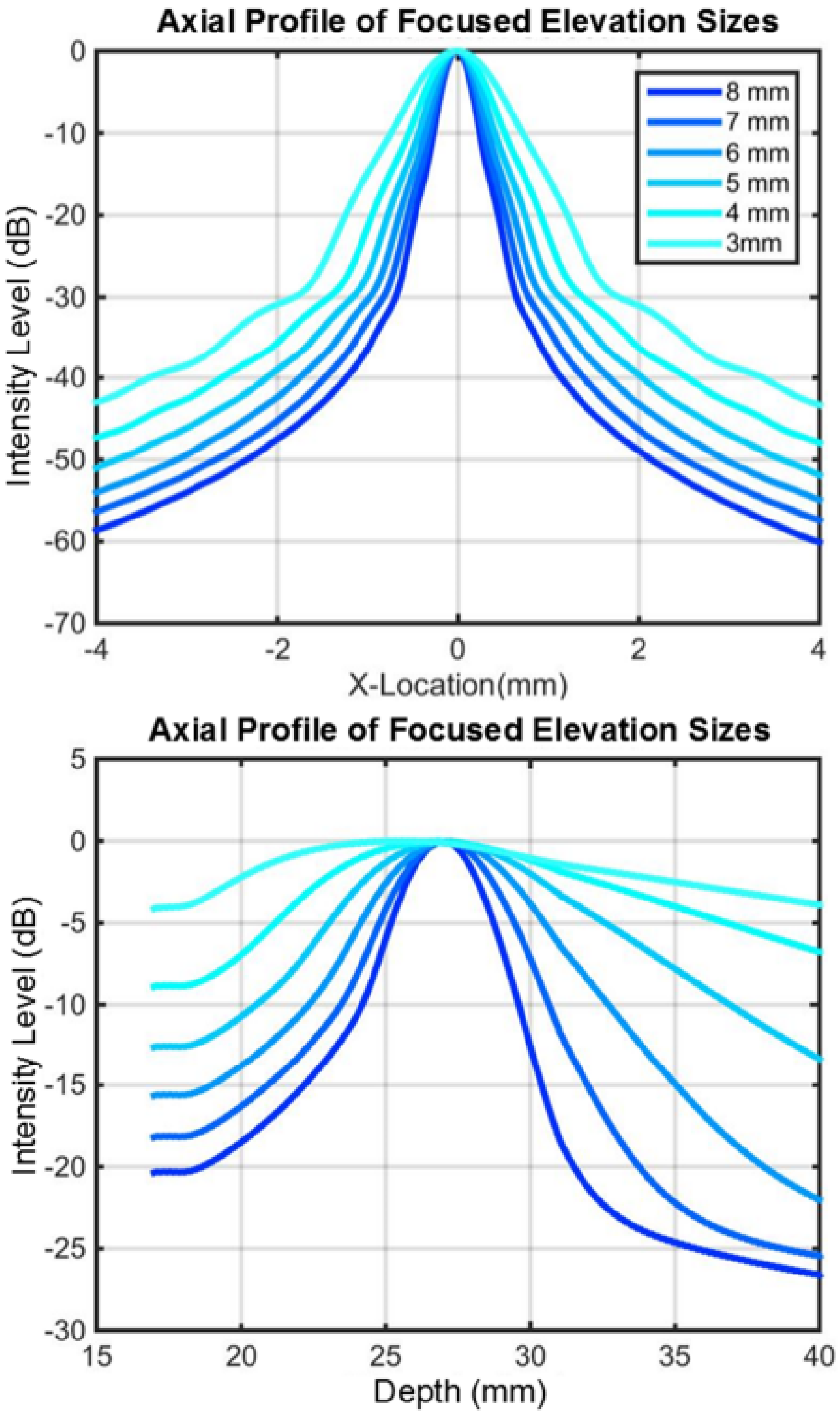

Figure 3.8 - A comparison of the difference between the focused for varying elevation sizes.

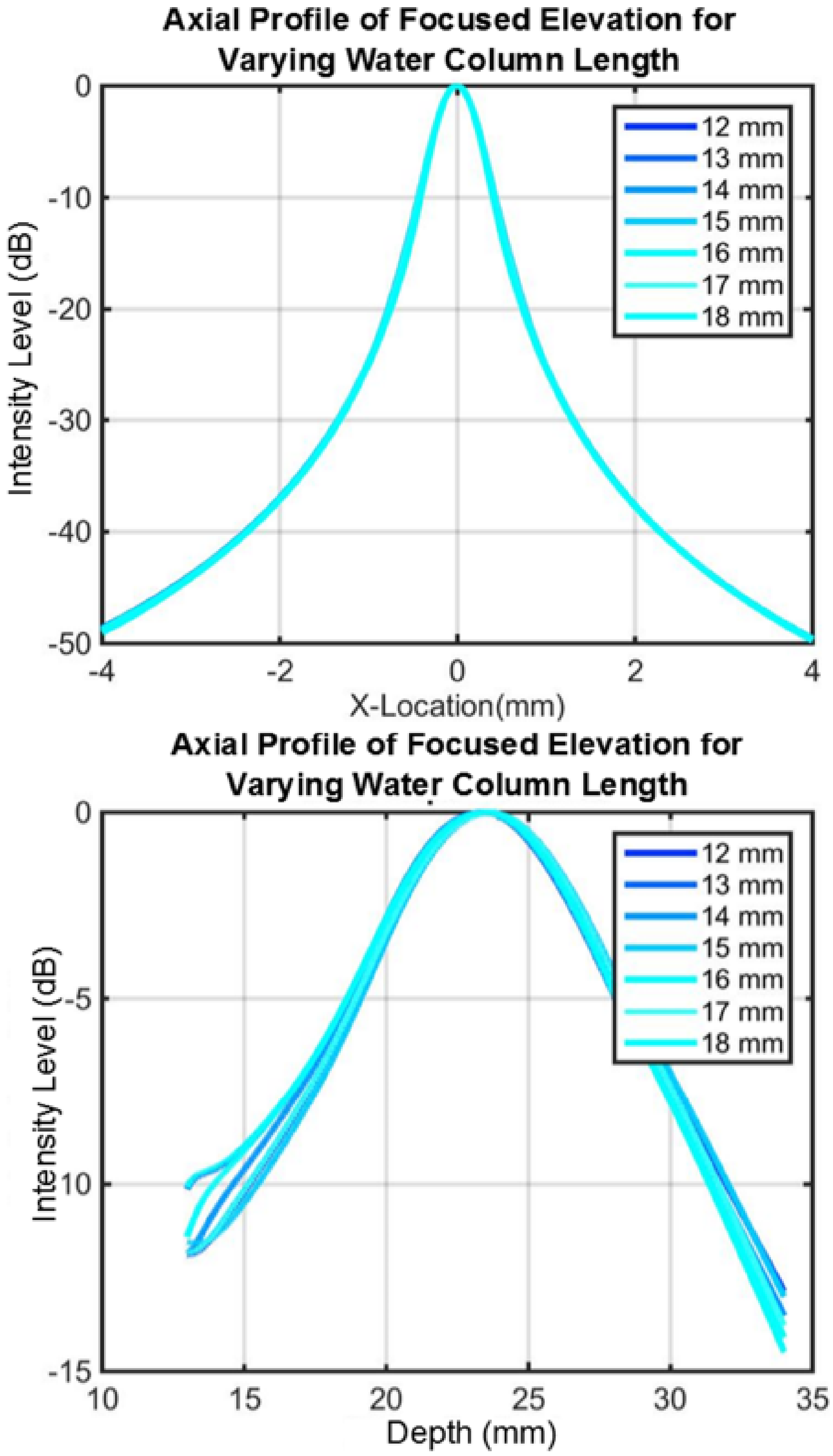

Figure 3.9 – Simulated results for a 5 mm elevation, with a varying size of water column.

3.4 Aperture and Element Sizing

Unlike the elevation focus, the electronically controlled aperture of the probe has far more relaxed constraints due to its ability to adapt to changes in the water and copper column lengths. The primary constraints on the focal length for the phased array portion of the probe were that it be capable of imaging the thickness of plates being welded with a single pass, meaning that the focal length would need to be approximately 5 mm in length. In order to achieve a focal point at the center of the system a minimum active aperture size of 5.6 mm was determined to be required using the far field estimation. To allow for multiple focal techniques to be explored and allow for grater focal abilities the aperture size was maximized within the system constraints, resulting in an 8 mm total aperture.

With the choice of aperture determined it became necessary to select the element size. Although theory states that the optimal focusing ability is achieved when the elements are chosen to be half wavelength in pitch the low steering angles used in this system allows for some reduction in this constraint. With this in mind it was decided that the transducer's elements would be chosen to be as large as possible without sacrificing imaging quality. Large elements, in addition to decreasing the system's cost have the advantage of greater homogeneity across the array. As the transducers frequency and amplitude are determined by the thickness and the size of the elements, decreasing the size of elements results in element sizes comparable to the allowed tolerance for the sectioning method, increasing inter-element variance. This larger size also decreases the likelihood that thinner or thicker sections of the material be sectioned into elements, decreasing the frequency variance between elements.

As most ultrasound systems make use of multiple 8 or 16 channel ADC boards it was decided to limit the total array to multiples of 8 elements. As before, each arrangement was simulated in both an on and off axes focus, the resulting profiles are shown in figure 3.10 and 3.11 for a range of 8 to 32 elements.

As can be seen in both the axial and lateral profiles of the probe, similar resolution profiles are obtained for all arrangements above 8 elements. As a result of this a 16 element probe was chosen, resulting in 0.45 mm elements with 0.05 mm spacing. This choice allows for a FWHM of 0.9 mm to be obtained when imaging the system.

With the dimensionality of the probe finalized a transducer whose specifications are listed in table 3.2 below, was ordered from Doppler Electronics Inc. It should be noted that the increase in active surface area of the probe should allow for an approximate 250% SNR increase. Coupled with the increased focal effects, this should allow for imaging in a far noisier environment than encountered in the laboratory.

Frequency	10 MHz
Number of Elements	16
Element Size	0.45 mm
Inter Element Spacing	0.05 mm
Elevation	5 mm
Pulse Duration	Minimal

Table 3.2 - The Specifications of the new phased array design

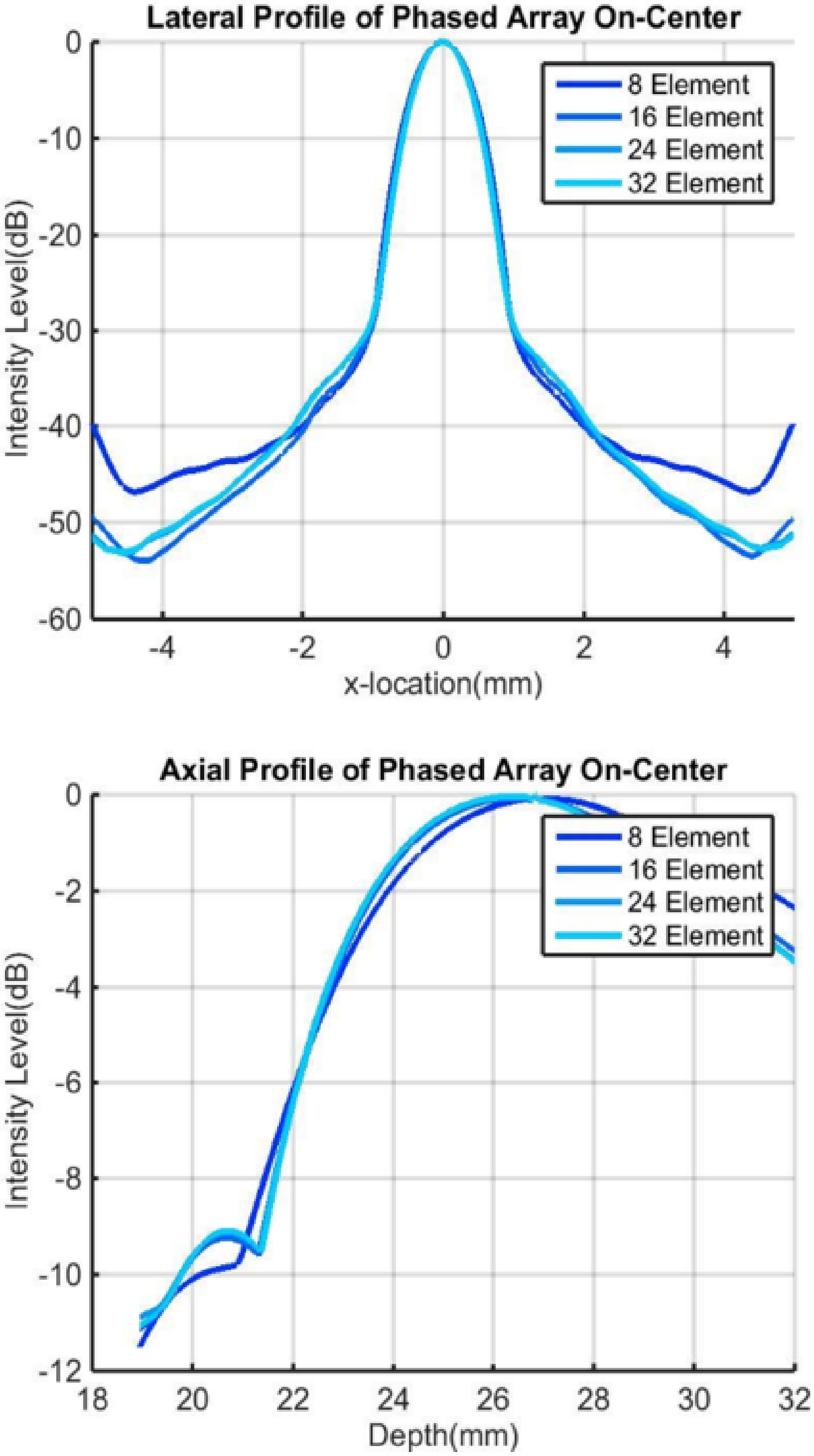

Figure 3.10 - The amplitude field profiles for an 8 mm active aperture with differing element sizes for an on-center focus.

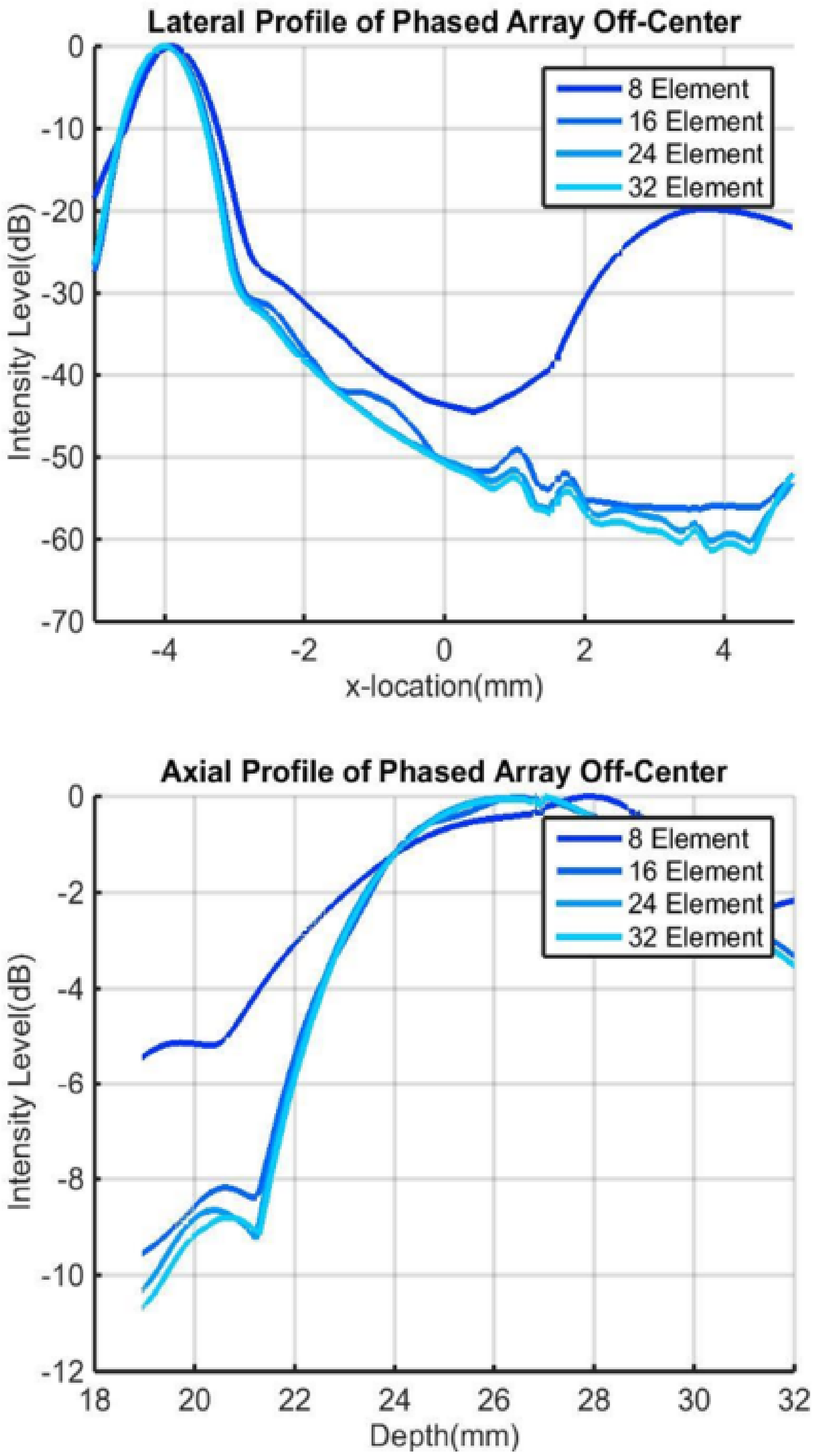

Figure 3.11 - The amplitude field profiles for an 8 mm active aperture with differing element sizes for an off-center focus.

3.5 Housing Design

Although the redesign was primarily performed to increase the imaging properties of the system, the housing was also modified. To allow for adaptation into an industrial test environment the system was designed to be adaptable to a range of electrode lengths. For initial testing a housing design was chosen to allow for disassembly and modifications as required. This housing consisted of a two part electrode with an internal holder that allows for positioning of the probe and directing the flow of water. In order to allow for disassembly the housing was threaded and a set screw used to prevent rotation after assembly. A low strength sealant was applied to prevent leaks and further strengthen the arrangement. The final dimensions of the housing were chosen to be 25.4 mm in diameter and 127 mm long with all tapers designed to comply with the specifications for our particular equipment. The geometry and final assembly is shown in figure 3.12, with minor modifications to this design made by technicians, including the thread size and the exact specifications of the internal holder.

This design was tested for its cooling ability using a phantom made from PEEK (a plastic capable of withstanding high temperatures.) This phantom was manufactured to the specifications of the ordered transducer and a cable was attached using epoxy adhesive. By integrating a thermocouple into the surface of the phantom the water temperature was monitored to ensure the safety of the piezo material. This setup was used to weld in a variety of extreme conditions, such as restricted water flow, rapid consecutive welds and extended weld times, with ground water (T = 20°C) providing the cooling. In these extreme conditions the surface temperature of the probe never exceeded 45 ˚C during operation. In addition, the housing was not found to leak during this process. Due to the severity of the conditions tested it was determined that the housing should have no issues providing adequate cooling in an industrial environment.

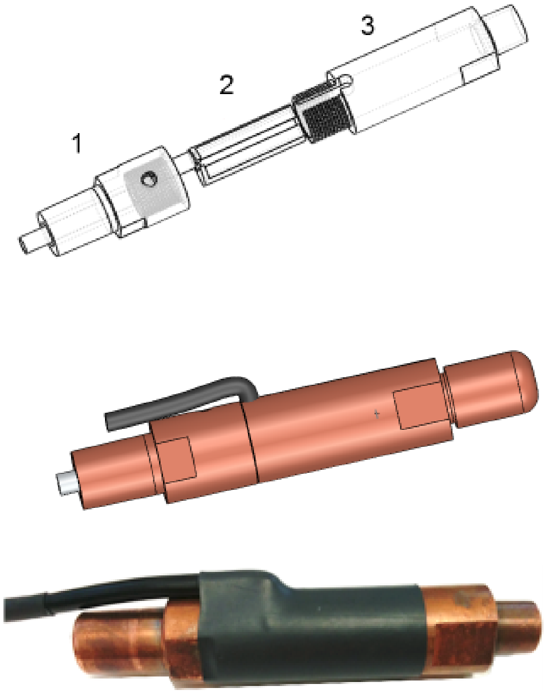

Figure 3.12 - The transducer housing design showing internal (2), external (1&3) designs and the resulting product from top to bottom

Although this design worked well, damage did result during the disassembly of the system. This resulted in the outer cable jacket of the transducer being torn and a repair being required. Future designs could prevent this by placing a small metal band on the cable to decrease stress on the joint. Although this may require the use of additional sealant between the surfaces this should not be difficult to implement. As future designs would be more permanent in nature a non-threaded setup, combined with an ultra-high strength sealant may be more desirable. If this option is chosen a brass housing may be desirable in order to prevent damage to the tapers that can occur with long term use. In addition to these modifications the hole used to route the cable should be placed at a higher angle of entrance to prevent damage during operation and ease external routing.

3.6 Electrode Cap Considerations

The primary concern with the copper cap in the past was the high attenuation of the sound wave passing through it. As this distorts the waveform and decreases resolution care must be taken to minimize the attenuation that the wave experiences. This attenuation has been measured within our group for a variety of copper alloys. It was found that GLIPDCOP (a specific alloy mixture of copper) allowed for noticeably lower attenuation due to the smaller grain sizes of this particular alloy. For this reason this alloy was chosen for this work.

In addition to the issue of attenuation other imaging artifacts can occur due to the geometry of the copper cap and the fact that the medium is dry coupled. The presence of the dry coupled media and the water copper boundary result in large reflections occurring of any wave incident upon them. Due to the high pulse repetition frequency (PRF) of the scanning system this can result in the reflections from these boundaries appearing in subsequent scans. This effect must be reduced by the proper choice of PRF for the system such that the reflections within the medium do not line up or do so at such a time that sufficient energy has been lost such that they are negligible.

In the simulations the copper has been considered a planar boundary. Due to the fact that this edge is coupled to air it is in essence a perfect reflector and can result in a large portion of the energy returning to the transducer at a time comparable to the desired target. Although this effect has been seen in scans near the edge of the weld cap the fact that it is relatively static means that filtering may be possible. If this filtering is not performed than care should be taken when examining the frames acquired within these regions.

3.7 Ultrasound Acquisition System

In order to acquire the data used in this research the Ultrasonic Open Platform[5] (Ula-OP) phased array system was employed. Ula-OP is an open platform that allows for the implementation of many focusing techniques and possesses the capability to store raw ultrasound data, meaning that it is a viable platform for the reception of full matrix data. Ula-OP is capable of addressing up to 64 independent channels and 192 elements through a 1-3 multiplexer arrangement. As all probes investigated were well below this limit there is no limitation in the focal patterns that can be employed. In order to allow for the driving of an industrial phased array the use of the high voltage pulsar board was employed, although capable of bipolar pulses of up to 160 V peak to peak negative square wave impulses were employed. Although this limited the voltage maxima to 80V this was not found to inhibit imaging in any way and allowed for a comparison to the majority of industrial phased array systems.

Ula-op allows for a maximum sampling frequency of 50 MHz, allowing for a 25 MHz Nyquist limit. Although an increased sampling frequency allows for simpler interpolation methods to be employed in focusing and a lower signal to noise ratio this sampling rate is sufficient to sample the selected probe at 250% bandwidth, meaning no loss of image quality should occur. At this sampling frequency both 8 bit and 12 bit data can be collected from the ADC boards and stored into a 1GB raw data buffer. It was decided that 12 bit data would be optimal for this research due to the wide range of amplitudes that exist between boundaries in question. In order to optimize image quality within the spot weld region, amplification was set to an amount such that prior to closing the jaws of the weld gun the copper air boundary is not saturated. As this impedance mismatch is the maximum that can occur within the system any reflected signal after this point should not be saturated.

Ula-OP allows for a scan repetition rate of up to 25 kHz, however high pulse repetition frequency (PRF) result in multiple reflections from within the copper structure. In an attempt to minimize these reflections a scan rate of 6700 Hz was chosen, this allows for the reflections to be minimal while allowing for the spot weld process to still be considered stationary during a single frame.

3.8 Experimental Verification of Resolution

Simulations allow for the visualization of many parameters, but they are inherently limited to both the underlying equations and the approximations made. Due to the approximations made in this case, mainly the lack of attenuation, and the relatively high tolerances allowed in manufacturing an experimental verification of the simulation results was desired.

In order to perform an experimental validation of the model a line spread phantom was designed. A line spread phantom works by making a sufficiently small line reflector within the imaged material, which when imaged is equivalent to the modeled 2D response, allowing for direct measurement of the resolution of a system to be made. Although the line spread phantom was desired to be as accurate a representation of the system as possible the coupling between copper and steel resulted in an amplitude distribution that is polluted with the reflection from the copper steel boundary, making direct comparison difficult. For this reason the line spread phantom was instead made from a copper rod matching the alloy used to manufacture the caps, with the total length of the copper being extended to maintain the imaging depth.

Measurements of this phantom were conducted using the full matrix capture method, the code for which can be found in Appendix A-D. This allows for an assessment of the resolution of both the old and new array. The resulting line spread functions were plotted on a normalized scale, seen in figure 3.13. The measured FWHM of both systems was determined to be 0.90 mm and 1.66 mm for the new and old system respectively. A comparison between the modeled and experimentally determined response for the new probe is shown in figure 3.14, the maximum difference between the two did not exceed 7% of the peak amplitude within the acquired data.

Although a determination of the effect of elevations lensing was desired this was not performed due to the fact that a line spread measure cannot be performed. This measurement could be performed in future work through the use of multiple copper phantoms. By machining slots into the phantoms and measuring the difference between the total reflected amplitudes of varying slot widths a profile of the amplitude can be obtained. This was not performed in this work due to the fact that the caps used had to be machined by hand and the tolerances were too low to allow for such a comparison.

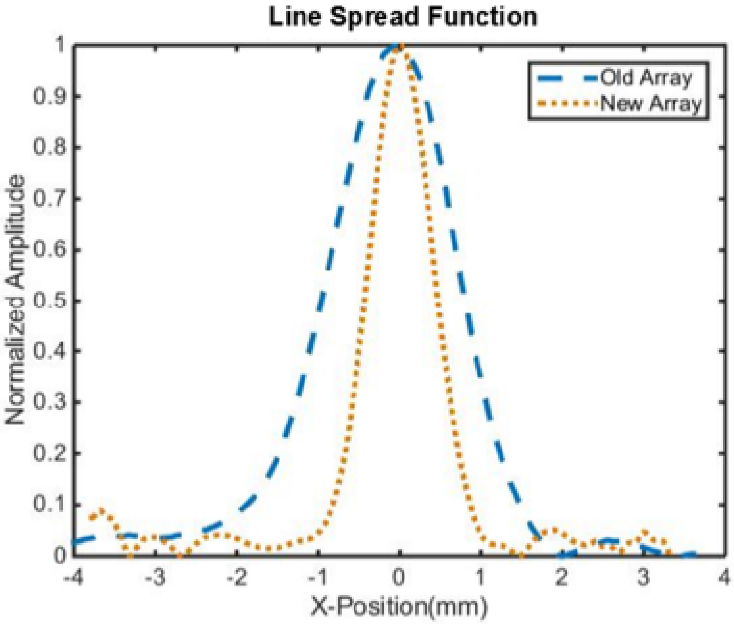

Figure 3.13 - The response function of both the new and old transducer to a line spread phantom. As is clearly seen the new transducer has a significantly higher focus than that of the previous system.

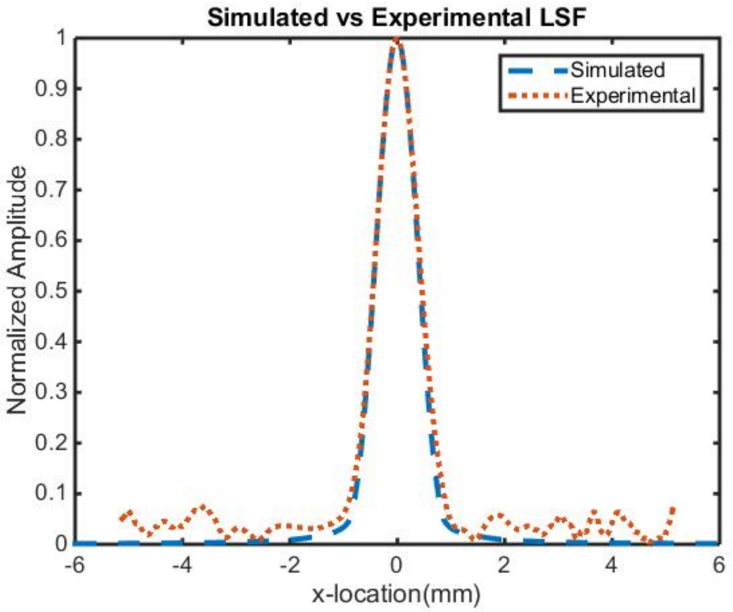

Figure 3.14 - The line spread function of the copper phantom compared to its simulated response in copper. The difference between the experimental and theoretical amplitudes does not exceed 7%.

The temporal resolution of the system after beamforming can be directly related to the axial resolution of the system. Although this resolution is influenced by both the pulsar used to drive the transducer and the manufacturing process it is important to determine. Temporally the transducer was found to undergo a slight lengthening of the impulse after beam forming occurred. The resulting wave, shown in figure 3.15 was found to have a total pulse duration of 1.5 wavelengths at its -6 dB point. As this impulse length is not optimal it may be desirable to optimize the electrical impulse used to excite the probe, as this could potentially reduce the length of its response.

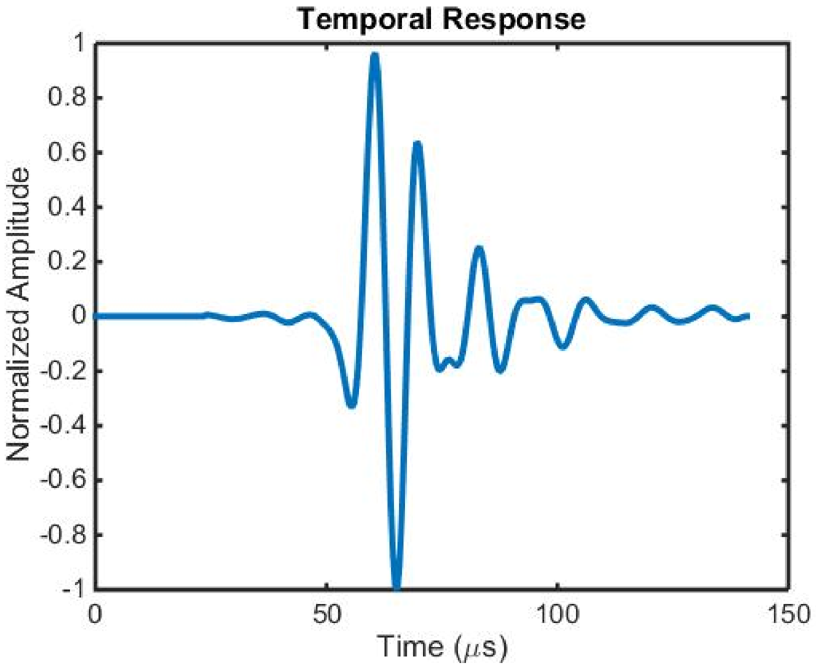

Figure 3.15 - The pulse duration of the signal after beamforming. A long duration of the signal indicates a ringing of the transducer occurs after initial excitation.

A measure of its linearity was also experimentally obtained. The linearity of a system determines how its response behaves across the region of measure. Due to the fact that in the spot weld system multiple linear boundaries are present waves incident at an angle will have a much lower transmission coefficient and will undergo deflection. In order to measure this factor a flat copper boundary was imaged. This boundary should yield a representative analysis of how the amplitude of the system would vary when imaging any flat boundaries after this point. As shown in figure 3.16 this non-linearity results in a decrease of the effective imaging area to approximately 6 mm in the new system. As this measure depends mostly upon the angle of incidence between the wave and the boundary its effects can be decreased by increasing the distance between the array and the boundary or using a smaller subset of the elements, however the corresponding decreased resolution should also be noted when doing this.

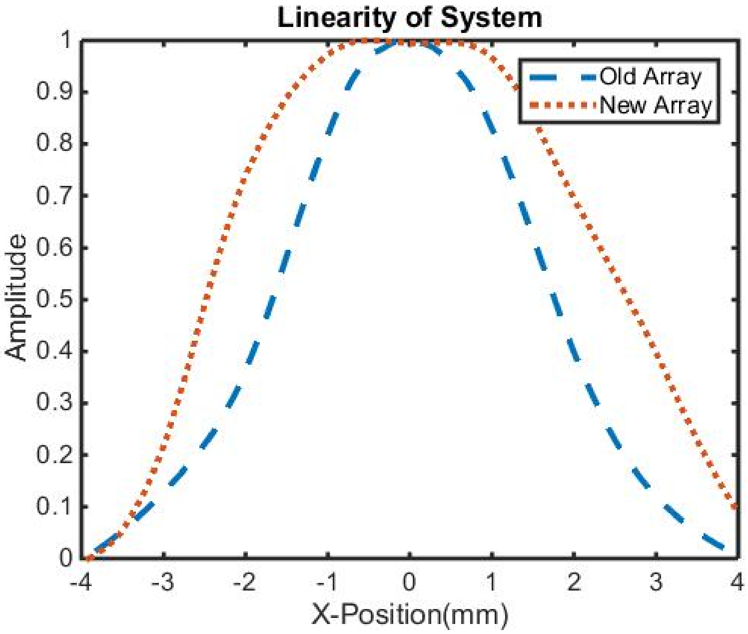

Figure 3.16 - A measurement of the linearity of the new and old system measured from a flat planar boundary. Both systems exhibit nonlinear intensities within the region of interest

References

[1] P. Kustron, J. Kocimski, A. M. Chertov, S. Titov, M. Korzeniowski, A. Ambroziak, R. Gr. Maev. *In-Line Ultrasonic Investigation of SPOT Weld Quality Using Multi-Transducer Set-Up*. IEEE Transactions on Ultrasonics Ferroelectrics and Frequency Control, DOI: 10.1109, (2005).

[2] Lui, Anthony, *Development of an Ultrasonic Linear Phased Array System for Real-time Quality Monitoring of Resistance Spot Welds*. Electronic Theses and Dissertations. Paper 4826. (2012).

[3] Bruce W. Drinkwater, Paul D. Wilcox, *Ultrasonic arrays for non-destructive evaluation: A review*, NDT&E international vol. 39, pp. 525-541 (2006).

[4] Brigham Young University, *ABCD Matrices Tutorial*, Retrieved from

http://www.photonics.byu.edu/ABCD_Matrix_tut.phtml

[5] P. Tortoli, et al., *ULA-OP: An advanced open platform for ultrasound research*, IEEE Trans. on UFFC, vol. 56, no. 10, (2009).

Chapter 4

Thermal Effects on Wave Propagation

In the spot weld process large thermal gradients are created within the media, primarily as a result of heat being transferred out of the object being welded. Due to the speed of sound's dependence on the temperature of the media these gradients result in a change in both the transmitted and received wave. These effects both degrade the quality of the image obtained and allow for determination of weld quality. Before analysis can occur on any imaged weld the artifacts introduced by the gradients must be understood. This chapter attempts to quantify the effects of the thermal gradients on imaging and determine methods by which weld quality can be determined in phased array systems.

4.1 Gradient Effects in Water and Copper

4.1.1 Phase Aberrations and Wave Superposition

In phased array imaging it is regularly assumed that the medium being imaged is of a constant sound speed. This assumption allows for the calculation of delay laws to be analytic, but results in small phase errors accumulating in each of the transmitted waves. These phase errors result in an amplitude distribution that is modified when compared to the original. Depending on the degree to which these errors accumulate severe losses of both resolution and accuracy can occur. Although in most cases these errors are small enough to allow for imaging to occur it is important to understand and quantify what errors may result from this assumption.

Finite element modelling allows for the determination of the phase errors and their effects so long as the material properties of the underlying medium are known. In the case of the spot weld process the temperature dependent density and elastic constants of water, copper and steel can be found in material databases. This, coupled with the existing spot weld model, will allow for finite element methods to be employed in the analysis process.

In order to determine the temporal offsets that occur, an inverse solution method was implemented. During focusing the goal is to generate a point source response at the intended position within the medium. By instead simulating a point source radiating from the intended target the exact delays necessary to focus at that point can then be calculated by the time of flight difference between elements. As this time of flight is the same for both transmission and reception the necessary delays for the total focusing method can be calculated by summing the elements pairs in question.

To allow for a direct comparison between the results of the modelled data both a thermally constant and a thermally varying media, shown in figure 4.1 were simulated. In order to maximize the effects of the gradients the profile was extracted from the end of welding. In each situation point sources were placed from -3.75 mm to -0.25 mm along the copper/steel boundary in steps of 0.5 mm. Due to the symmetry of the system and the previously determined resolution this allows for the time of flight to be determined at any point using interpolation and symmetry. In the case of the thermally constant media the modelled time of flight was found to agree with the calculated time of flight (using the MATLAB function in Appendix B-D) to within the discretization of the model’s time step, indicating low numerical error produced using this technique.

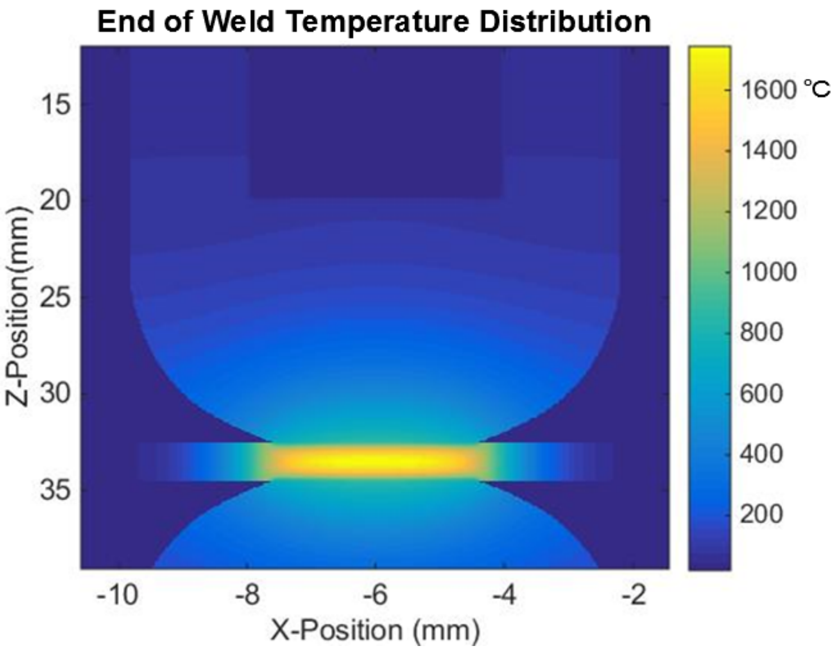

Figure 4.1 - The temperature profile extracted at the end of welding using previous numerically modeled weld. Weld was simulated using 8 kA applied for 20 cycles.

By taking the difference between the two acquired times of flights the time of flight difference can be found. This difference, seen in figure 4.2 indicate that the wave undergoes a shift of between 0.3 and 0.8 wavelengths when both travel directions are accounted for. Although this change will result in a displacement of the wave, this difference contains both the phase and group delay of the wave as it propagates. In order to determine the effects of the phase delay the difference between individual elements within the array can be plotted. This difference, shown in figure 4.3 reveals that the majority of the phase delay difference occurs towards the edge of imaging system. For each simulated point, the wave transmitted from the element will arrive out of phase by an amount corresponding to the phase delay. As this occurs on both transmission and reception the net phase error for each transmit/receive pair will have a phase error corresponding to the sum of the individual element’s phase error.

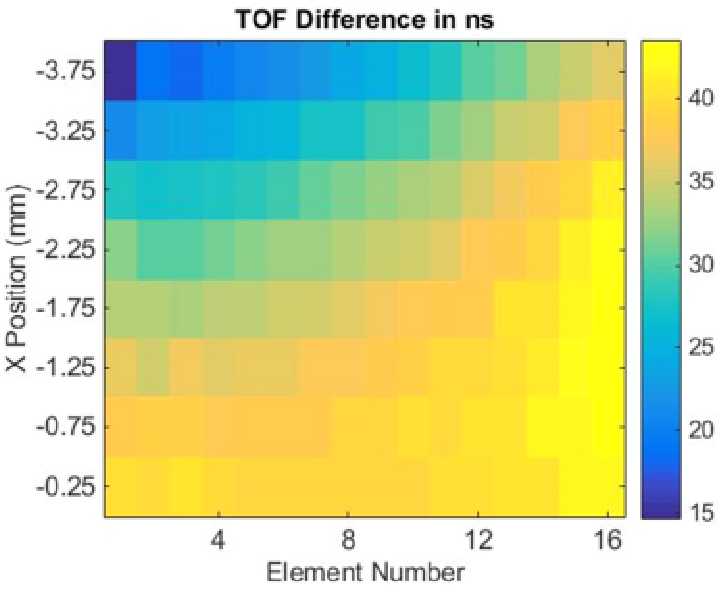

Figure 4.2 - The time difference between a thermally constant and thermally varying media. The difference is notably proportional to both the heating along the trajectory and the length of the trajectory.

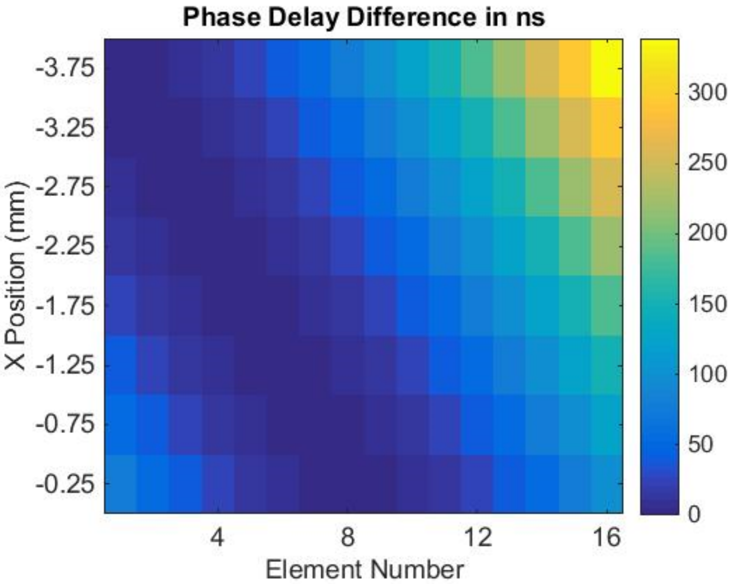

Figure 4.3 - The phase delay difference associated with the time of flight difference, the difference in the phase delay increases as the focal points move away from the center of the media.

In order to approximate the effects of these offsets on the waveform the phase errors for the central and furthest off axes point were used to calculate the corresponding phase errors associated with them. In an idealized array each element has no directivity, meaning that for a point source reflector located at the focal point the effect of phase errors can be found through the summation of the transmitted waveform with an applied phase offset corresponding to each of the transmit receive pairs. In the case of the system used here this results in the addition of 256 waves with each combination of phase offsets from figure 4.3 applied. When this is performed the resulting waves in figure 4.4 are obtained. Although degradation in the amplitude of the wave was found to occur this 15% reduction in amplitude should not prevent imaging from occurring. As offsets in the wave position can be corrected using general affine transforms this means that the effects of phase error can be ignored during the imaging process.

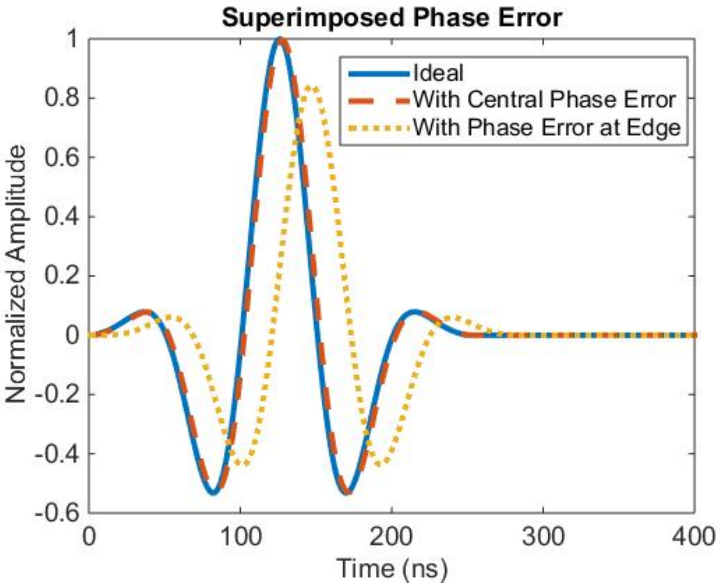

Figure 4.4 - The waves resulting from the summation of ideal point sources with the phase delay offsets applied. The resulting waveforms indicate that at the edge of the imaging field a reduction of 15% in amplitude would occur in a worst case scenario. It should be noted that the temporal shift of the wave can be corrected for in post processing.

This method can be used to yield a good estimate of the thermal offsets, but it is inherently limited in the fact that it relies on the use of a model to determine the effects. This means that for each material and welding schedule the effects will inherently change by some amount. For this reason it is desirable to measure the effects of the offsets experimentally as the weld occurs. Due to the fact that full matrix capture allows for the pre-beamformed data to be acquired it provided the greatest possibility for experimental determination. In order to investigate this possibility simulated data was acquired using the full matrix capture technique and the same thermal distribution use in the previous model. This allows for any decoupled results to be compared with the exact phase offsets.

In the acquired data the waveform will be the original signal convolved with the response function of the system. As a result of this convolution not all points of data can be reliably used for time of flight determination. The best candidates for determining the time of flight between individual elements and a point in space are elements directly above the imaging point and element pairs whose trajectory crosses the center of the imaging region. In this aim the data from these elements was acquired for comparison to the corresponding time of flights. As the time of flight to and from the intended target is the same, the total time of flight is simply halved in each case.

When this modelled data was examined the time of flight between an element and itself was found to be in good agreement with the desired results, however the time of flight across the center was found to have a large error associated with it. This was found to be due to the geometric effects of the copper cap. In this case the tapered edge acts as a secondary reflection, which when added together with the planar reflection off of the copper surface results in an unintended lensing effect. With this lensing effect removed through a matched layer the differences were found to be significantly reduced, however, extrapolation of values to the entire array's offsets produced values whose error is larger than the offset due to the gradients.

It was therefore determined that although the individual element measures do give good relation to the thermal variations within the media, the measurements made using full matrix capture cannot be used to determine or correct for the phase errors introduced.

4.1.2 Simulated Results of focal spot changes

In addition to the changes in the delay patterns, simulations can also be used to determine how the directionality of the resultant wave will be modified. Using the forward approach and modelling the propagation of the waves using the original delays allows for an estimation of the spatial dislocation of the wave from its intended target. By comparing the amplitude distribution at the end of the copper medium the wave's location can be found with respect to its intended target. This can be seen in figure 4.5 below, along with the axial profile of the waveform. From the simulations a small 0.205 mm offset from the intended target is found to occur as a result of both the copper and water gradients. In the case of the spot weld process such a small shift is well below the tolerances of measure and should in no way affect the results.

Although small gradients within the media will result in slight shifts from the intended location, the primary source can be determined by examining the amplitude ratio of the two waves. In this case it is noted that the amplitude of the wave with thermal gradients present is 17% greater than the original. The speed of sound in heated copper allows for a slightly higher focus to be achieved, but does not account for this change, indicating another source.

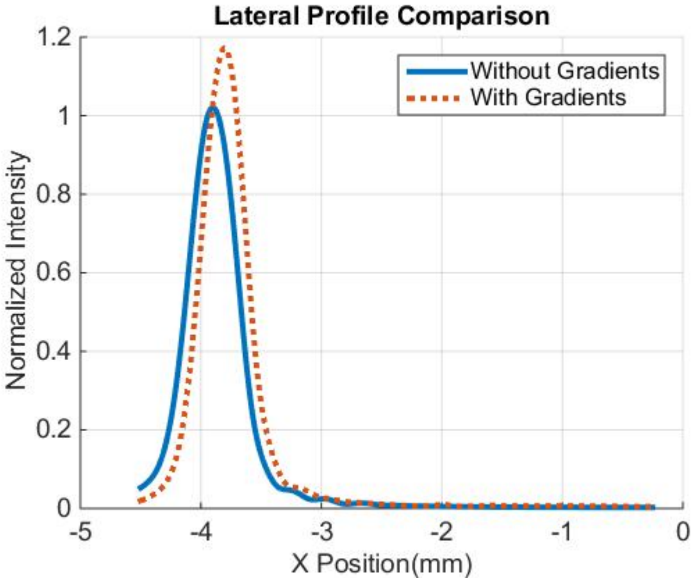

Figure 4.5 - The change in amplitude and position of the beam emission pattern, as normalized to the pattern with no gradients present.

The primary source of this change can be found through examining the coupling effects between water and copper as the temperature increases. By examining the change in transmission amplitude, seen in figure 4.6 it was found that 88% of the amplitude change was accounted for. In addition to the change in the reflection coefficient, the angle of refraction at this boundary will also change in relation to the speed of sound ratio shown in figure 4.7. To determine how much of the offset is attributable to this, the angle of trajectory from the center of the array was calculated and its final position determined using Snell's law and trigonometry. When this was done the total offset caused by this change was determined to be 0.173 mm, meaning that both the amplitude and positional variations are primarily a result of the boundary between the media heating. This means that knowledge of the copper water boundary temperature would be sufficient to compensate for any changes that might occur prior to the wave reaching the imaging region.

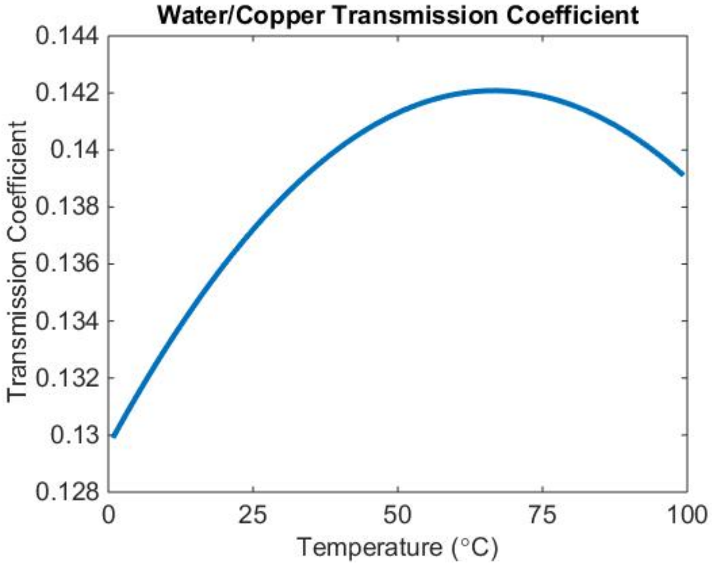

Figure 4.6 - The transmission coefficient between water and copper as a function of temperature for a perpendicularly incident wave. As temperature increases a greater portion of the incident wave in transmitted in the region of modeled temperatures

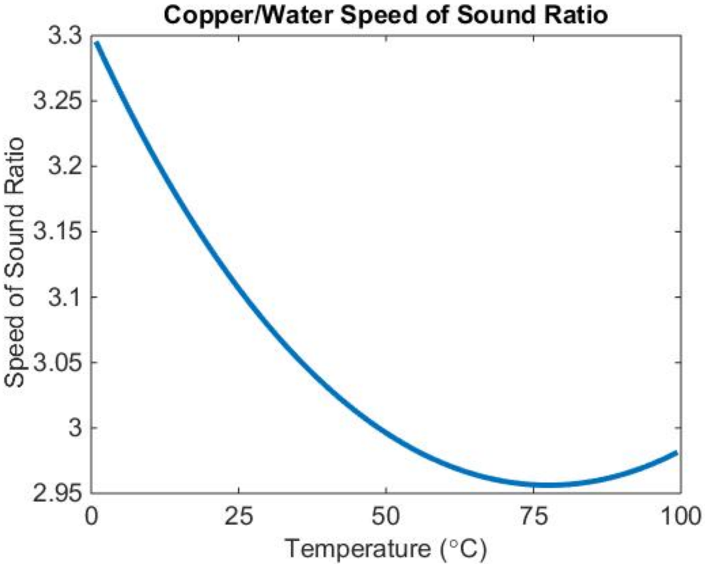

Figure 4.7 - The speed of sound ratio between water and copper as a function of temperature. Through Snell's law it can be noted that an increase in temperature will lower the angle of transmission, resulting a wave whose final position is closer to the center of the weld nugget.

4.2 Effects of the Steel Boundaries

Unlike the water copper boundary, the copper steel boundary undergoes a much larger increase in temperature. This temperature change is offset by the fact that the speed of sound decreases with temperature in both media, resulting in a boundary whose speed of sound ratio remains relatively unchanged during welding, as shown in figure 4.8. This indicates that the wave's trajectory change is dependent only on the copper water boundary in the welding of steel. As the dimensionality of the system remains constant any changes can therefore be corrected using standard affine transforms.

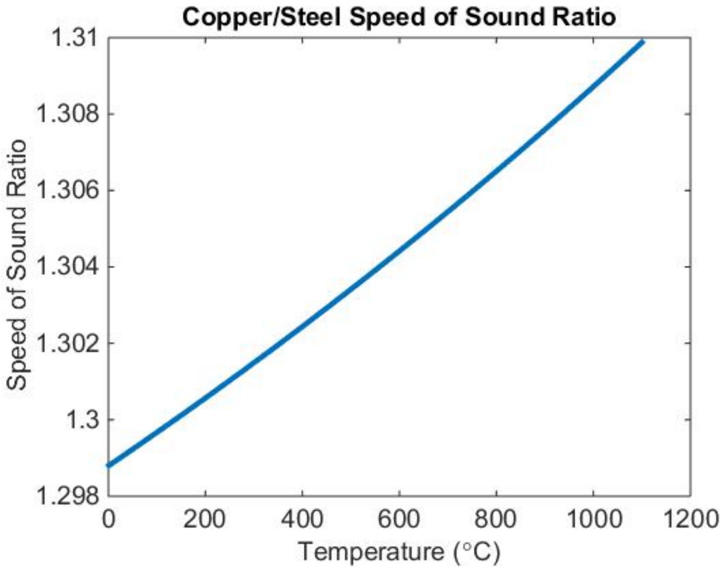

Figure 4.8 - The speed of sound ratio between a copper/steel boundary as a function of temperature. Very little change is indicated through the range in which copper is solid and the transmission angle is dependent almost solely upon the incident angle.

In a similar way, the impedance mismatch (figure 4.9) between the boundaries remains relatively constant. Due to the presence of the dry coupling between the copper and steel, the primary change in amplitude at this boundary will therefore be due to the change in the coupling conditions resulting from increased deformability of the media. Although this fact should allow for an additional measurement parameter, the computation of this change is made difficult by the change in the transmission coefficient at the copper water interface and the growth of the molten metal resulting in overlap between the two reflections. Any determination of quality based on amplitude will therefore have to factor in these effects.

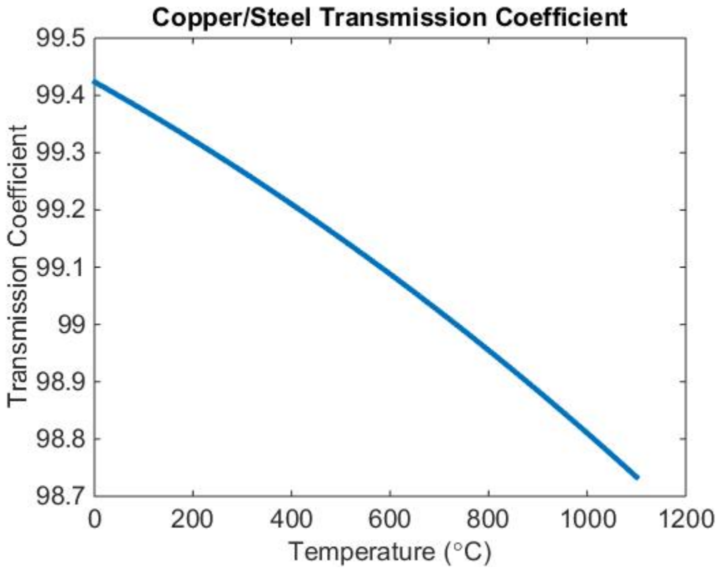

Figure 4.9 - The transmission coefficient between copper and steel as a function of temperature. The transmission coefficient is essentially unchanged over the temperature range for which copper is solid. This indicates that any change in the reflected wave from this boundary will be due to the change in coupling due to an increased deformability.

Although the copper/water and copper/steel boundary remain essentially static in space throughout the welding process the formation of a molten nugget creates a dynamic boundary which depends primarily on the welding conditions. At this boundary the ability to determine the presence of molten nugget in each frame depends primarily on how the nugget forms within the metal. As the model used in this experiment neglects contact resistance the nugget growth is primarily from the center of the metal sheets in an oblong shape, however, this is not always the case in experimental situations. In all cases the refraction through the weld nugget interface is a result primarily of the contact angle and the speed of sound ratio between the media. Since this ratio is constant at the interface the resultant angle of transmission can be found using Snell's law, graphed in figure 4.10.

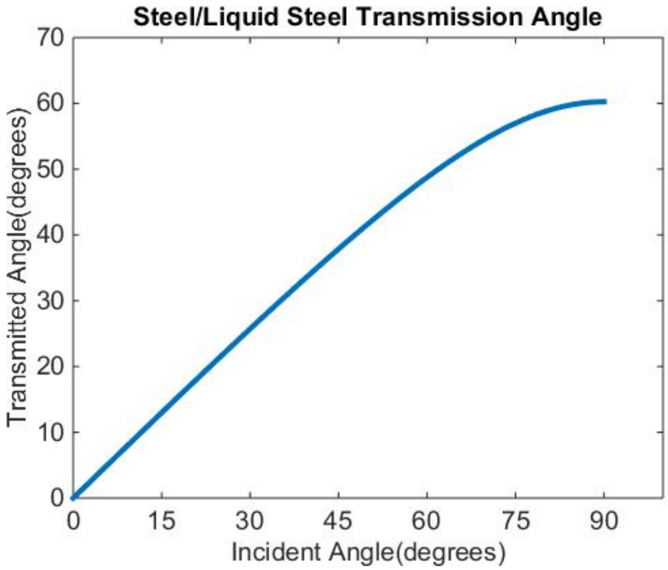

Figure 4.10 - The change in angle a wave will experience when intersecting a molten nugget. The fact that the angle of transmission is roughly half that of incidence means that reflections from inside of the molten pool may be affected during the early stages of molten growth.

By performing the cross sections using differing welding currents and times a visualization of the growth of the molten metal pool can be performed. Knowing the shape of the molten metal pool allows for descriptions of how the molten metal will deflect sound through it. In doing this a good estimation of how the weld will influence ultrasonic data can be acquired. Due to the variety of weld schedules and the influence that material thickness can have on spot welding, particularly in non-symmetric setups, not all cases can be covered in this work. For this reason this work shall be limited to symmetric cases, although predictions in non-symmetric cases should be easy to do in the future.

In a symmetric welding situation the primary influence on nugget shape is the heating rate in the bulk material and at boundaries. As mentioned in theory, the contact resistance is influenced primarily by the surface contact conditions during welding. In order to reduce the heat generation at these points slow heating can be used to soften the metal and increase coupling prior to welding[1]. When this is done the boundary conditions within the system are nearly identical to the modeled condition and results in the formation of elliptical nuggets from the center of the sheets. If heating is continued the nuggets growth will eventually result in an oblong shape due to the copper electrodes on both sides of the weld acting as heat sinks.

In the other extreme, contact resistance can be the primary source of energy input into the system. In these cases, lower force and higher currents are used. When this happens the resulting nugget growth tends to be rectangular in nature and in the most severe cases result in hourglass shapes forming between boundaries. Depending on the input parameters the early stages of heating also result in the formation of small expulsion sites and increase the likelihood of voids forming.

The final nuggets imaged in this thesis were oblong or rectangular, however theory allow for a discussion of all effects. In the cases of oblong nuggets or square nuggets the molten metal grows from the center of the weld start and expands outward. In these cases molten metal growth will result in high deflection of waves after passing though the molten pool. After the weld has reached sufficient size a near planar boundary results and distortions will be decreased, meaning that measurement should be limited to after this point. Prior to the development of a large liquid nugget both deflection from the surface of the pool and reflection from the bottom of the pool result in waves whose trajectory will be highly modified. Due to this fact the phased array imaging system will likely be unable to image the spot weld growth when the nugget is much smaller than the total thickness of the sheets, meaning that quality determination must rely on other techniques.

4.3 Experimental Results of Scanning

Experimental determination of the predicted offsets result posed fundamental issues due to the fact that most of the predicted effects were below the accuracy of the measurement techniques available. In addition, the predicted changes are coupled together with other effects in the system, limiting analysis outside of small measurement ranges.

Prior to examining the effects of the gradients the system's noise level was analyzed. In order to do this a static system, in this case the surface of the copper cap, was imaged repeatedly. The noise of the system was measured by comparing individual frames within the spot weld setup prior to welding. As the system should be static at this point each frame should be the same. The original data and this variance, seen in figure 4.11, indicates that the electrical noise of the system is well below the acquisition range, however turbulence within the water column results in small shifts of the boundary position during the acquisition process. Note that as this acquisition is pre-beamformed data, electrical noise in the final image will be reduced even further.

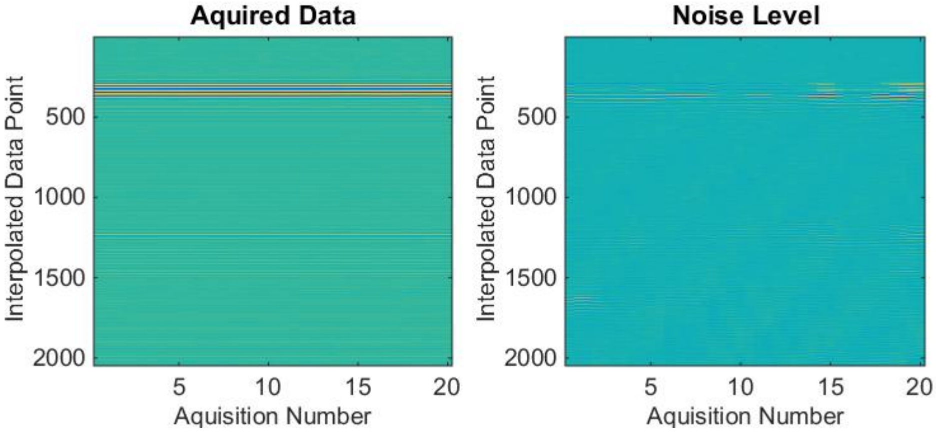

Figure 4.11 – A plot of data collected from the system prior to welding and the corresponding noise. Although electrical noise was found to be negligible in the acquisition process small shifts in the position of the transducer results in minor shifts to the boundary position, introducing some variance in the reflections position within the image.

Visualizing the amplitude of the copper/steel boundary during the welding process did of course correlate fairly well with the heating of the medium. As can be seen in figure 4.12, the boundary's amplitude did decrease as heating occurred and the deformability of the media increased. During the heating and subsequent melting process it was found that a 75% decrease in the amplitude of the reflected wave occurred prior to the heating of the water copper boundary. After heating had stopped, cooling resulted in a shrinkage of the molten pool and a loss of coupling between the media, as seen at the 670 ms mark. This loss indicates that measurement of any subsequent reflections should occur prior to this point, as loss in coupling was seen to result in poor imaging quality.

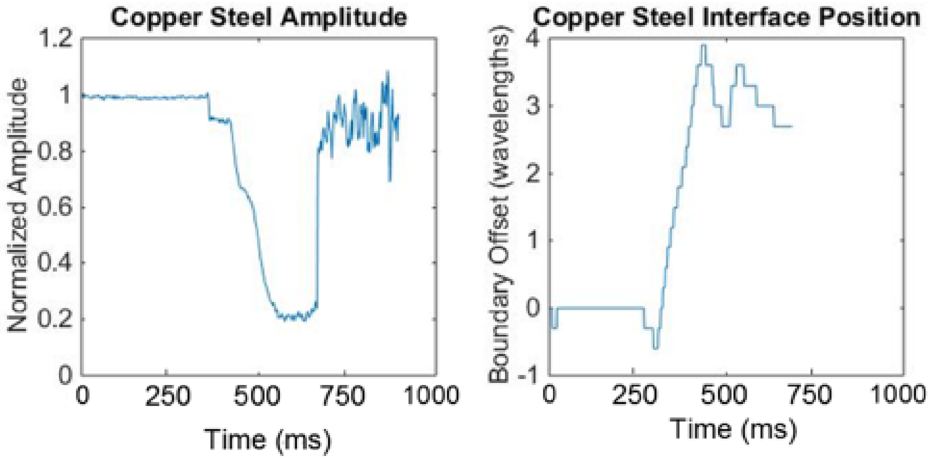

Figure 4.12 - A depiction of the time evolution of the copper steel boundary amplitude and position. The amplitude of the reflection was found to significantly decrease as the steel plates heated, eventually reaching a minimum.

During this research many of the welds performed using short weld times and high current resulted in the presence of multiple voids and the lack of fusion between the molten pools. Although these cases are undesirable in a welding environment the fact that the arrangements are unique allow for a measurement of the position of these defects using the phased array system. By comparing these images to offline methods an estimation of the offsets caused by thermal gradients can be performed. Although these voids and regions of disbonding allow for the potential to measure the thermal offsets, the error associated with the measurement techniques must be understood in order to allow for proper quantification.

Cross sectioning allows for high resolution images to be obtained, however the accuracy of such a method in determining the position of voids within the media and the size of the weld is inherently limited. The primary source of this limitation is the fact that cross sectioning involves both cutting and polishing of the spot weld. If cutting does not occur along the exact center of the weld then the cross section will under predict weld size. Additionally, defects such as small voids have to potential to appear undersized and in severe cases the performed cut can remove the portion of the weld with voids present. When the cross sectioning is performed the potential also exists to break weak bonds between the plates, as these weak bonds are acoustically transparent this will result in a disagreement between the cross sectional and acoustic data.

Acoustic microscopy, unlike cross sectioning, allows for the entire bonded structure to be examined. This has the advantage of allowing for a much closer comparison to data acquired using the phased array device. One of the primary difficulties in assessing acoustic microscope data is the fact that stick welds can appear acoustically transparent to ultrasound. Although this factor can be remediated by applying a force to the welded structure using a mallet, it does produce some error in the measurement of features.

Acoustic microscopy allows for a more accurate profiling of the acoustic properties of the weld and better comparison to the data acquired with the phased array. Despite this, analysis is made difficult by both the differing resolution and the fact that unlike acoustic microscopy, the phased array has an inherent nonlinearity. When data is acquired with the phased array system, disbonding will be greatly influenced by non-linearity, meaning that the amplitude of reflections from lack of bonding will have a position dependent amplitude similar to that of figure 3.16. Unlike disbonded regions, small voids within the media will act as point source reflectors and not be limited by this non-linearity. As the presence of both voids and disbonding occurred in the examined welds the reflections from the combinations of these structures will appear in the phased array data. This combination, and the resolution limitations of the system must be considered for any comparison that occurs.

In order to estimate the thermal offsets that occur data from each of the 3 methods was acquired for comparison. As the reflecting structures such as void will have formed by the end of solidification comparison to offline techniques can be performed. This B-scan, shown for a particular weld in figure 4.13 shows the reflections from both copper electrodes and from between the steel sheets. Any voids or lack of fusion will occur at the boundary between the steel plates, shown at an imaging depth of approximately 30 mm. By extracting the amplitude profile of this boundary, plotted in figure 4.14, the position of any reflectors can be compared to the cross sectional and acoustic microscope images of the same weld (figure 4.15 and 4.16 respectively).

To compare the acquired profile to the cross sectional data the location of the reflectors was plotted on a binary scale, with 0 representing a bond and 1 representing the presence of a reflector. In the case of acoustic microscope data the average for a 1 mm window along the center of the scan was plotted. A 1mm window was chosen to increase correlation with the array data, as the elevation profile will result in the collected data using the phased array to be an average response over a region of approximately this size in the elevation direction. The comparison of the 3 differing profiles, shown in figure 4.17, show good agreement between the acoustic microscope, cross sectional and array data, with no notable thermal offsets observed. It should be noted that one of the primary issues in the comparison between the acoustic microscope data is the non-linearity of the system. This decay results in measurement being limited to reflectors within the central portion of the weld and has the potential to skew the measured offsets towards the center of the imaging system.

In all examined case the offsets of the reflections between the acquired data was between 0.0 mm and 0.5 mm. As previously discussed a wide variety of factors affect the error for each comparison, meaning that the error will vary in each acquired data point. Although varying, the error in all cases is higher than the associated measure of the offsets, with an average error in measure of approximately 1 mm. This makes verification of the modeled results impossible. Although this means that the associated measure cannot be used to determine the thermal offset, the measurement does indicate that the phased array system should be capable of determining the presence of voids and disbonding to a good degree during the welding process.

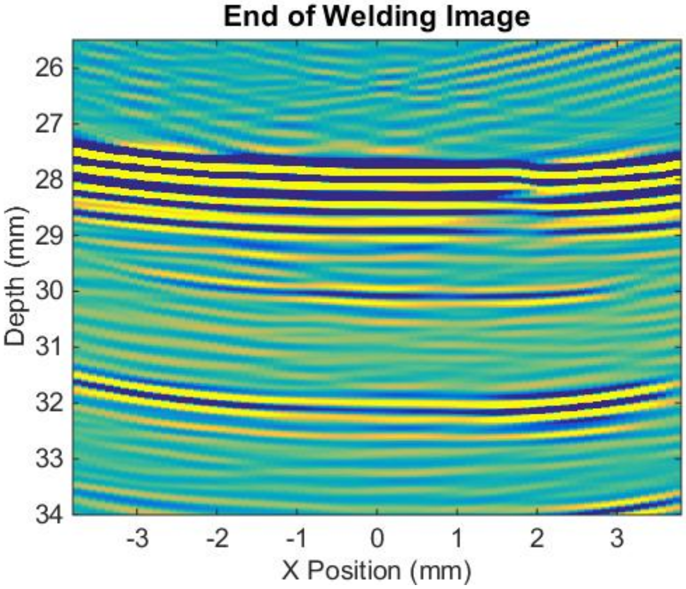

Figure 4.13 - B-scan acquired at the end of solidification. At the end of heating a clear curved appearance is present in the interfaces. This curvature is indicative of lower angle trajectories being remapped to higher values, as the wave is expected to travel further than they do.

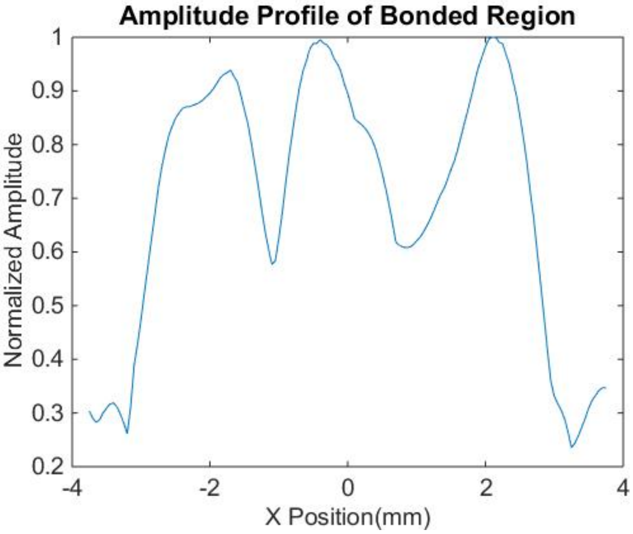

Figure 4.14 - An amplitude profile along the final weld piece. The reflections from the edges appear to be over predicted by approximately 0.5 mm on each edge. This indicates that the modelled effects are occurring, however the error associated with measure means that such conclusion is not definitive.

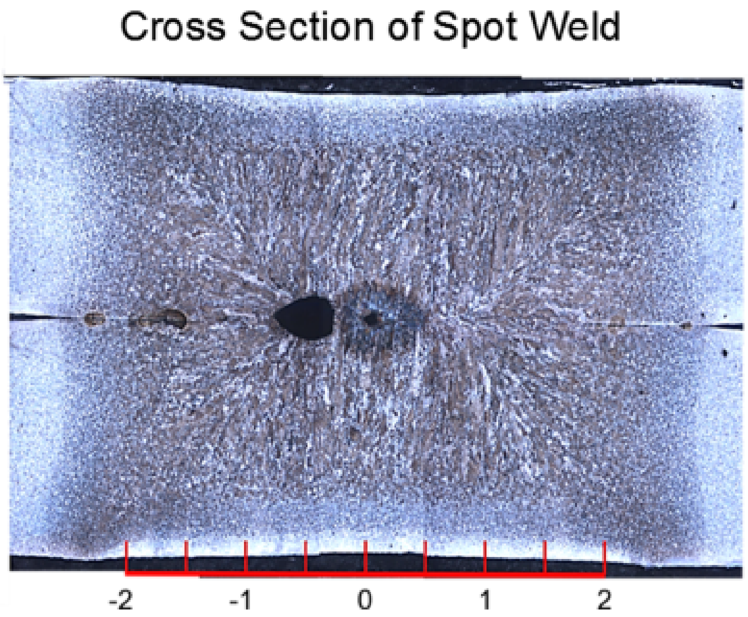

Figure 4.15 - A cross sectional view of the weld. Cross sectioning reveals that the final location of the unbonded region is approximately 1.5 mm on both sides of the nugget.

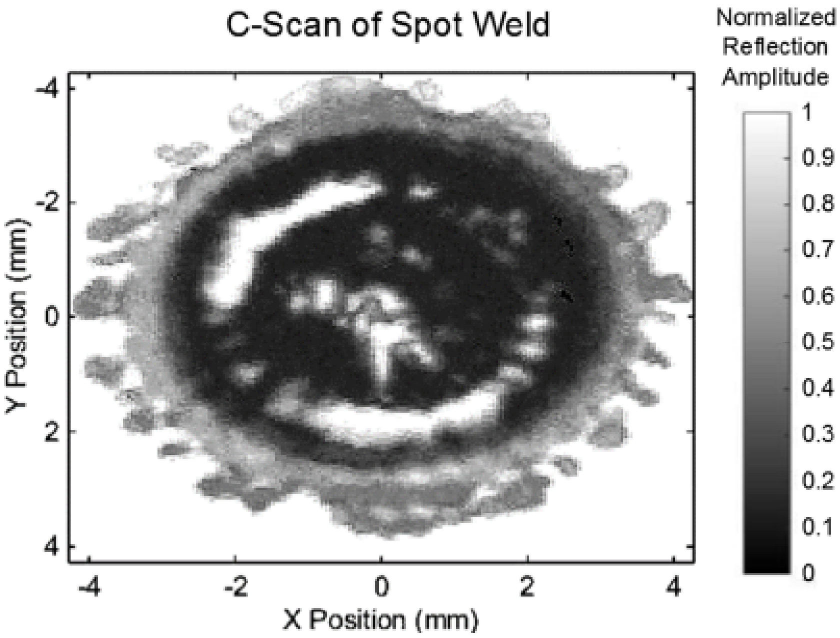

Figure 4.16 - The acoustic microscope image of the weld. Scanning of this plate during welding is taken at the Y-axes origin. Bonded area is estimated using the darkest region. A high variance was found to result when compared to the cross sectioned image due to the presence of a weak bond around the edge of the weld.

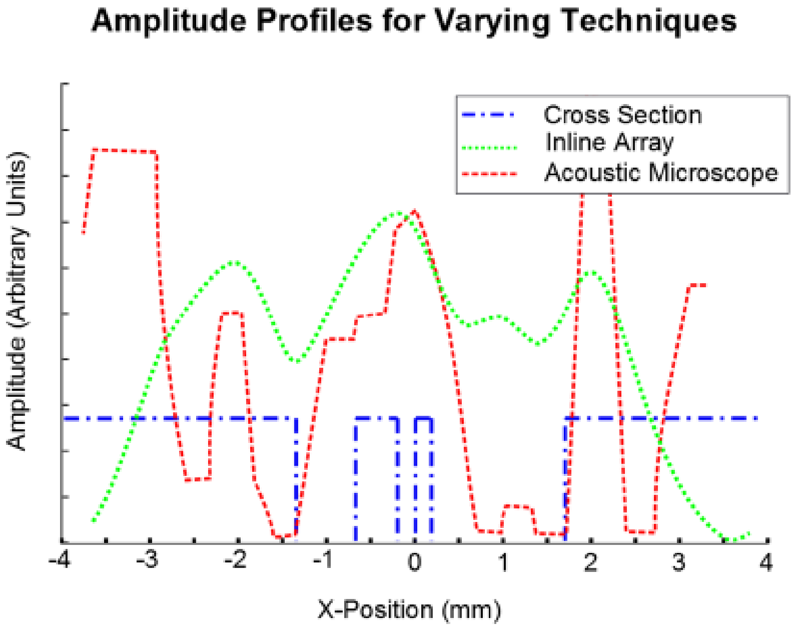

Figure 4.17 – A comparison of the extracted profile from each of the methods used. Although data acquired with acoustic microscopy correlates well with the inline device the resolution difference and non-linearity of the imaging system have a large influence on comparison results.

In addition to these measurement, examination of the boundary profiles in both pre and post heating can yield information about the presence of thermal offsets within the system. If thermal offsets are generated during the welding process the profile of static boundaries such at the copper/steel boundary will have a tendency to acquire a curvature, as the decreased angle of propagation will result in the reflected boundary appearing sooner than expected in the image. Comparing the profiles at the start and end of welding, shown in figure 4.18 and 4.19, reveals no notable difference in the perceived curvature of this boundary.

In both situations the acquired experimental data indicates no notable offsets due to thermal gradients. These results indicate the thermal gradients should have no notable effect on the imaging process.

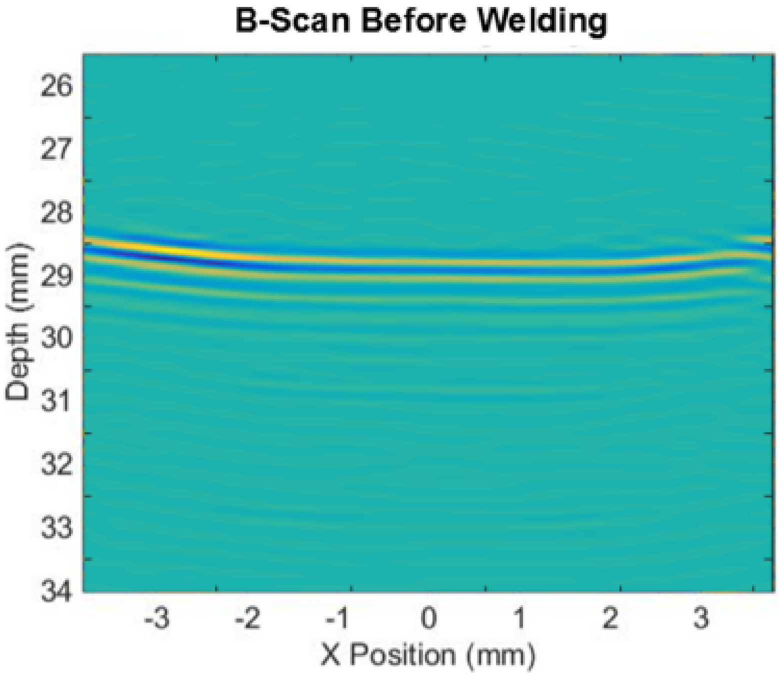

Figure 4.18 - The acquired B-scan prior to the start of welding. A small curvature towards the edge of the image indicates that the geometric structure of the electrode has some influence in these regions.

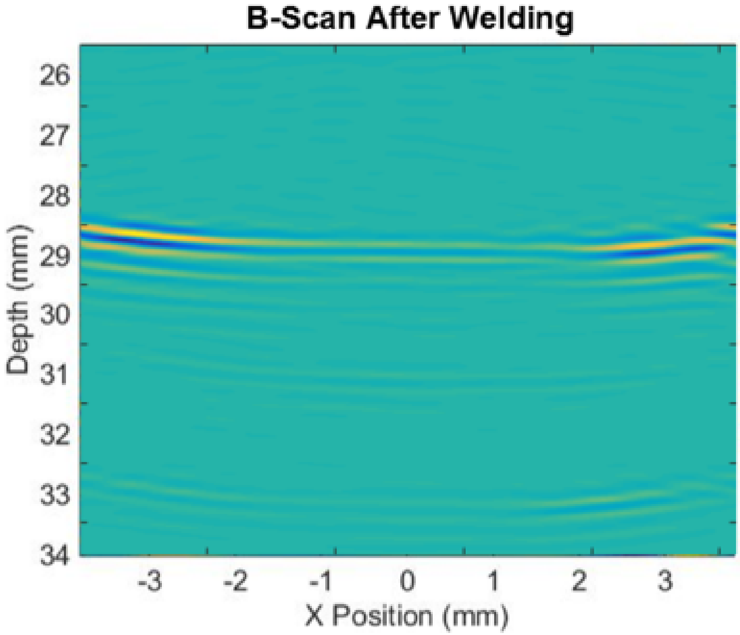

Figure 4.19 – The acquired B-scan at the end of welding. Although increased coupling has resulting in a change in the copper-steel boundary amplitude no increase in the curvature of the boundary is present. This indicates that the resulting thermal offsets have no notable effect on the acquired image.

References

[1] Rogeon PP, Raoelison RR, Carre PP, Dechalotte FF. *A Microscopic Approach to Determine Electrothermal Contact Conditions During Resistance Spot Welding Process*. ASME. *J. Heat Transfer,* (2008).

Chapter 5

Summary and Future Work

In this work I completed a redesign of the phased array imaging system intended for inline spot weld quality assessment. By using ultrasound imaging principles I was able to achieve a resolution that was double that of the previous system without increasing the imaging frequency. In addition to this I designed an implementable lensing system that allows for a resolution increase of 250% in the elevation direction. This allows for the acquired image to be processed with the assumption that it was taken along the central cross section of the spot weld. A more implementable housing was also designed, allowing for ease of implementation into existing environments. Finally a 15 MHz version of the array was designed for future testing, allowing for an additional 50% gain in resolution on top of those previously mentioned.

In addition to this redesign process I performed an investigation of the effects of the thermal gradients produced within the spot weld process. The results of this show that the effects of the gradients on the imaging process result in a negligible phase error being associated with the collected data, meaning that existing phased array devices can be used for the acquisition of data. In addition to these phase errors I determined that a small spatial offset of the wave results due to the heating of the copper water interface. This heating generates a deviation from the angle predicted using Snell’s law and results in a 0.2mm offset from the intended position occurring at the edge of the imaged system. Although this introduced error is negligible in most cases, it can be compensated for by monitoring the temperature of the water copper boundary and applying affine transforms to the resultant image.

With the results of this work it was found that imaging with the phased array system should be possible in many of the cases where the single element device is currently employed. By supplementing or replacing existing monitoring systems more accurate spot weld quality measure should be possible in a real time manner to an accuracy of approximately 0.9 mm, with additional resolution achievable using the 15 MHz array.

In order to perform these measures various development work is still required, mainly the algorithms that can be employed to assess weld quality. These algorithms and the validation of their accuracy must be performed for a large variety of materials, including aluminum welding and dissimilar welding. As these are the primary areas where the implementation of the single element device has proved difficult, significant work will likely be required. By performing this additional research it is possible that the phased array device will become widely employed in situations where welds are considered critical, allowing for a decrease in the time required to manually assess weld quality.

APPENDICES

Appendix A – Total Focusing Matlab Code

```
%% Define Tranducer Properties
probe.num_elements = single(16);
probe.active_apeture = single(16);
probe.element_pitch = single(0.5e-3);
probe.frequency = single(10e6);
probe.bandwith = single(.65); %
probe.bandwith = single(0.6*ones(1,16));
probe.sensitivity = single(ones(1,16));

%% Define Focal Grid
fgrid.x_start = single(-3.75e-3);
fgrid.x_end = single(3.75e-3);
fgrid.x_resolution = single(0.5e-3);

fgrid.z_start = single(28e-3);
fgrid.z_end = single(34e-3);
fgrid.z_resolution = single(.24e-3);

%% Define Imaging Media
medium.sound_speed = single([1480, 4960, 5890]);
medium.thickness = single([15.6e-3,11e-3]);
medium.bound1 = single([0, 15.5e-3, .01e-3]);
medium.bound2 = single([0, 25e-3,0e-3]);
%% Create Computation Grid
fgrid.x = linspace(fgrid.x_end,fgrid.x_start,round((fgrid.x_end-fgrid.x_start)/fgrid.x_resolution))';
fgrid.z = linspace(fgrid.z_start,fgrid.z_end,abs(round(fgrid.z_end-fgrid.z_start/fgrid.z_resolution)));

%% Define Transducer Locations Within Grid
% create element locations
probe.element_locs = single(linspace(-
.5,.5,probe.num_elements)*probe.element_pitch*probe.num_elements);

%% Calculate Delays for Focusing
%expand computational domain
fgrid.x = repmat(fgrid.x,[1,size(fgrid.z,2),probe.num_elements]);
fgrid.z = repmat(fgrid.z, [size(fgrid.x,1),1, probe.num_elements]);
probe.element_locs = repmat(permute(probe.element_locs,[1,3,2]),[size(fgrid.x,1),size(fgrid.z,2),1]);

% calculate active apeture
if (probe.active_apeture < probe.num_elements);
   temp1 = probe.element_locs-fgrid.x;
   [~, active_elements] = sort(temp1,3);
   active_elements = active_elements(:,:,1:probe.active_apeture);
```

```
    %resort to fix ordering
    active_elements = sort(active_elements,3);
else
    active_elements = repmat(permute(1:probe.num_elements,[1,3,2]),[size(fgrid.x,1),size(fgrid.z,2),1]);
end

%prealocate delays and angles of focusing
theta = single(zeros((size(fgrid.z))));
tof = theta;
%calculate delays for point within the water column
%determine points in this space
tpoints = (fgrid.z<=(fgrid.x.*medium.bound1(3)+medium.bound1(2)));
theta(tpoints) = atan(fgrid.x(tpoints)./fgrid.z(tpoints));
tof(tpoints) = sqrt((fgrid.x(tpoints)-
probe.element_locs(tpoints)).^2+fgrid.z(tpoints).^2)./medium.sound_speed(1);
%calculate delays for points within copper column
%determine points in this space
tpoints = (fgrid.z > (fgrid.x*medium.bound1(3)+medium.bound1(2))) & ...
    (fgrid.z <= (fgrid.x*medium.bound2(3)+medium.bound2(2)));
[theta(tpoints) , tof(tpoints)] = findAngleSlope(probe.element_locs(tpoints),single(0),...
    fgrid.x(tpoints),fgrid.z(tpoints),[0,medium.bound1/2,0],medium.bound1, ...
    [medium.sound_speed(1),medium.sound_speed(1:2)],single(1e-5));
%calculate Steel Column
tpoints = (fgrid.z > (fgrid.x*medium.bound2(3)+medium.bound2(2)));
[theta(tpoints) , tof(tpoints)] = findAngleSlope(probe.element_locs(tpoints),single(0),...
    fgrid.x(tpoints),fgrid.z(tpoints),medium.bound1,medium.bound2, ...
    medium.sound_speed,single(1e-5));
%% Read in Full Matrix Data
%this section is completely device dependant
% In order to perform TFM imaging we must first aquire FMC data, this is
% stored by Ula-Op as a file, which must be read into memory.
%use a gui interface for file selection
%[FileName,PathName] = uigetfile('*.rff12','Select the bft file');
% Here we specify how many recievers are present using Ula-Op
DataObj1el=DataUlaopPreBeamforming(strcat(PathName,FileName),(1:16)');

SetOffsetPri(DataObj1el,16); % this tells the class that we have 16 emissions to complete a frame

Read(DataObj1el,'firstPri',1,'npri', 25000); %Read in 25000 ascans, number can be adjusted


[nGate,nCh,nPri]=size(DataObj1el.LastReadData); %extract the number of gate, channels and the number
of pris

ula.timedata =
DataObj1el.LastReadData(:,:,1:probe.num_elements*(floor(DataObj1el.LastReadPri/probe.num_elements
)));
ula.t_dims = size(ula.timedata);
```

```
ula.timedata = reshape(ula.timedata, [ula.t_dims(1),ula.t_dims(2), ula.t_dims(2),
ula.t_dims(3)/ula.t_dims(2)]);

ula.t_dims = size(ula.timedata);
if length(ula.t_dims) <4
   ula.t_dims = [ula.t_dims 1];
end
% create the time array of the system, done by taking the sample
% number, deviding by the sampling frequency and adding to this the delay
% before recording starts.
ula.time=DataObj1el.LastReadTime(1)+(0:nGate-1)/DataObj1el.fs;
ula.initdelay = (DataObj1el.uop.item0.rxsettings.rymin.num*1e-
3)*2/DataObj1el.uop.workingset.soundspeed.num;
ula.time = ula.time+ula.initdelay;
ula.fs = DataObj1el.fs;
clear nGate nCh nPri
%% Apply TFM using a simple sum
%Interp FMC data to 200 MHz, such that nerest nieghbor is an okay
%approximation
interp_factor = 4;
%zero mean data
ula.timedata = ula.timedata-repmat(permute(mean(ula.timeda,1), [1,2,3,4]),[ula.t_dims(1) 1 1 1]);
%Interpolate
ula.timedata = interpft(ula.timedata,interp_factor*ula.t_dims(1),1);
te = repmat(active_elements,[1,1,1,probe.active_apeture]);
re = permute(te,[1,2,4,3]);
%collect the time of flight for each te,re and sum to get points
temp1 = (single(1):single(size(te,1)));
temp1 = repmat(temp1',[1,size(te,2),size(te,3),size(te,4)]);
temp2 = (single(1):single(size(te,2)));
temp2 = repmat(temp2,[size(te,1),1,size(te,3),size(te,4)]);
tof = tof(sub2ind(size(tof),temp1,temp2,te))+ tof(sub2ind(size(tof),temp1,temp2,re));
%switch TOF grid to index points in aquired data
index = ceil((1*ula.fs*interp_factor).*(tof-ula.initdelay));
%remove time of flights that are outside of aquired data
junk_data = (tof<ula.initdelay) | (tof > max(ula.time(:)));
index(junk_data) = 1;
%expand out indexes to cover all frames
te = repmat(te,[1,1,1,1,ula.t_dims(4)]);
re = repmat(re,[1,1,1,1,ula.t_dims(4)]);
index = repmat(index,[1,1,1,1,ula.t_dims(4)]);
s = size(index);
fn = repmat(permute(single(1:ula.t_dims(4)),[1,5,3,4,2]),[s(1:end-1) 1]);
%fetch data
ula.image = ula.timedata(sub2ind(size(ula.timedata),index,te,re,fn));
clear fn s index te re
%perform sum
ula.image = squeeze(sum(sum(ula.image,3),4));
```

Appendix B – Calculation of Angle and TOF though Media

```
function [theta_0,tof,x_3] = findAngleSlope(x_0,z_0,x_f,z_f,b1,b2,c,tol)
%find angle slope takes as input two sloped interfaces, an initial and
%final position the accoustic speeds of the media and the tolerance of the
%determined point in the x-direction. It returns the time of flight between
%these two points, as well as the trajectory angle of the final ray
%determine the distance between the second boundary and the final ray depth

%use a fan approach, starting with an angle of 180 degrees and decreasing
%by halves each time
theta_0 = zeros(size(x_0))+pi/24;
%now loop through until tolerance is met, or angle is rejected as
%impractical
%use getX3bound to determine the location of the initial guess(ie 0 degrees)
x_3 = getX3Bound(theta_0,x_0,z_0,z_f,b1,b2,c);
cond = (abs(x_f-x_3)<tol).*(imag(x_3)==0);%check tolerances
fact_i = pi/16;%adjustment factor for brute force approach
count = 0;
while(sum(~cond(:))>0)
%    count = count+1;
%    sum(~cond(:))
  %loop through factor in terms of factor step
  %for fact = (-fact_i:fact_i/2:fact_i);
  theta_0u = fact_i+theta_0;
  theta_0d =-fact_i+theta_0;
  %determine the position of all three possible angles
  x_3 = (getX3Bound(theta_0,x_0,z_0,z_f,b1,b2,c));
  x_3u = (getX3Bound(theta_0u,x_0,z_0,z_f,b1,b2,c));
  x_3d = (getX3Bound(theta_0d,x_0,z_0,z_f,b1,b2,c));
  %find the minimum deviation from ideal and assing new theta
  adjust_cond = (abs(x_3-x_f)<abs(x_3u-x_f));
  theta_0 = theta_0.*adjust_cond+theta_0u.*~adjust_cond;
  adjust_cond = (abs(x_3-x_f)<abs(x_3d-x_f));
  theta_0 = theta_0.*adjust_cond+theta_0d.*~adjust_cond;
  %check if condition has been met after this recursion
  x_3 = getX3Bound(theta_0,x_0,z_0,z_f,b1,b2,c);
  cond = abs(x_f-x_3)<tol;%check tolerances
  %adjust factor if not to be the smallest step size of previous recursion
  fact_i = fact_i/2;%.*fact_step;
  if fact_i == 0 || count >55
    cond = 1;
  end
  count = count+1;
end
%determine tof
[~,tof] = getX3Bound(theta_0,x_0,z_0,z_f,b1,b2,c);
tof = real(tof);
end
```

Appendix C – Calculation of Trajectory through Layered Media

```
function [x_3,tof,phi_1,phi_2,x_1,z_1,x_2,z_2,theta_1,theta_2] =
getX3Bound(theta_0,x_0,z_0,z_f,b1,b2,c)
%use the angle of the boundary and the initial angle to find the angle of
%intercept
phi_0 = getPhi(theta_0,b1(3));
%now use snell's law to find the angle of transmission
phi_1 = asin(sin(phi_0)*c(2)./c(1));
%convert this back into theta
theta_1 = getTheta(phi_1,b1(3));
%now use theta_1 to find the second intercept
phi_1 = getPhi(theta_1,b2(3));
%again apply snell's law
phi_2 = asin(sin(phi_1)*c(3)./c(2));
%again change it back
theta_2 = getTheta(phi_2,b2(3  ));



%we now have the theta angles at each boundary, we must now calculate the
%points of intersection between the rays and the boundaries, as these will
%be indicative of the final position.
[x_1,z_1] = getPoi(x_0,z_0,tan(pi/2-theta_0),[b1(1),b1(2),b1(3)]);
[x_2,z_2] = getPoi(x_1,z_1,tan(pi/2-theta_1),[b2(1),b2(2),b2(3)]);
%with this we now have the final trajectory of the ray, so it is a simple
%matter to compute where it would lay on the x plane
x_3 = (z_f-z_2)./(tan(pi/2-theta_2))+x_2;
%calculate the time of flight
tof = sqrt((x_1-x_0).^2+(z_1-z_0).^2)./c(1)+sqrt((x_2-x_1).^2+(z_2-z_1).^2)./c(2)+sqrt((x_3-x_2).^2+(z_f-
z_2).^2)./c(3);
%we now compare this value to the desired value, and accept or reject it.
%crit = (abs(phi_2)<asin(c(2)/c(3)))&&(abs(phi_1)>asin(c(1)/c(2)));
x_3((abs(phi_2)>asin(c(2)/c(3)))&(abs(phi_1)>asin(c(1)/c(2)))) = inf;
end
```

Appendix D – Code for Transitioning Between Coordinate Systems

```
function theta = getTheta(phi,m_bound)
% getTheta takes an angle phi taken from a boundary of slope m_bound and
% computes theta, the angle phi in an x,y cartesian system.
% if nargin > 2
%     error('Incorrect number of inputs');
% else
  %find the intercept of the two rays using dot product
  theta = atan((m_bound));
  theta = phi-theta;
%end
end
```

```
function phi = getPhi(theta_ray,m_bound)
% getPhi takes a ray and boundary and computes the angle between them, if a
% boundary is not defined it assumes a linear boundary, such that Theta=Phi
% if nargin < 2
%     error('Incorrect number of inputs');
% else
  %find the intercept of the two rays using dot product
  %phi = atan((tan(theta_ray)-m_bound)./(1+tan(theta_ray).*m_bound));
  %find the angle of the boundary from its slope
  theta_bound = atan(m_bound);
  %we know that the boundaries will have an angle between them of the
  %original plus this angle
  phi = theta_ray+theta_bound;
%end
end
```

VITA AUCTORIS

NAME: Andrew Ouellette

PLACE OF BIRTH: Windsor, Ontario

YEAR OF BIRTH: 1990

EDUCATION: B.Sc. [Honours] Physics
2013 University of Windsor, Windsor, Ontario

M.Sc. Physics, 2014
University of Windsor, Windsor, Ontario